The Dissertation Committee for Jinyang Liang certifies that this is the approved version of the following dissertation:

High-Precision Laser Beam Shaping and Image Projection

Committee:

Michael. F. Becker, Supervisor

Daniel J. Heinzen

James W. Tunnell

Brian L. Evans

Seth R. Bank

High-Precision Laser Beam Shaping and Image Projection

by

Jinyang Liang, B.E.; M.S.E.

Dissertation

Presented to the Faculty of the Graduate School of

The University of Texas at Austin

in Partial Fulfillment

of the Requirements

for the Degree of

Doctor of Philosophy

The University of Texas at Austin

May, 2012

Dedication

To my beloved wife, Jiajing Zhou.

Acknowledgements

I would like to express my gratitude to many people without whom I cannot finish this dissertation. First and foremost, my sincere thanks go to my Advisor and friend Dr. Michael F. Becker for his patient guidance, unfailing availability, encouragement, and all his many contributions to my research as well as the writing of this dissertation. In addition, I am grateful to Dr. Daniel J. Heinzen for his insights and support for my research. I also appreciate Dr. James W. Tunnell for many valuable discussions. Finally, I acknowledge Dr. Brian L. Evans and Dr. Seth R. Bank for their helpful comments and services as members of my dissertation committee.

I also would like to thank my laboratory colleagues Sih-Ying Wu and Rudolph N. Kohn for their assistance and helpful suggestions.

Finally, I would like to give my special thanks to family. I dedicated my work to my parents, Ping Zhou and Jingsha Liang, for their guidance and emotional support and for my wife, Jiajing Zhou who encouraged and helped me in many ways throughout the study.

Jinyang Liang

The University of Texas at Austin

Austin, Texas

March 2012

High-precision laser beam shaping and image projection

Jinyang Liang, Ph.D.

The University of Texas at Austin, 2012

Supervisor: Michael F. Becker

Laser beams with precisely controlled intensity profiles are essential for many areas. We developed a beam shaping system based on the digital micromirror device (DMD) for ultra-cold atom experiments and other potential applications. The binary DMD pattern was first designed by the error diffusion algorithm based on an accurate measurement of the quasi-Gaussian incident beam from a real-world laser. The DMD pattern was projected to the image plane by a bandwidth-limited 4f telescope that converted this pattern to the grayscale image.

The system bandwidth determined the theoretical limit of image precision by the digitization error. In addition, it controlled the spatial shape of the point spread function (PSF) that reflected the tradeoff between image precision and spatial resolution. PSF was used as a non-orthogonal basis set for iterative pattern refinement to seek the best possible system performance. This feedback process, along with stable performance of DMD, the blue-noise spectrum of the error diffusion algorithm, and low-pass filtering, guaranteed high-precision beam shaping performance.

This system was used to produce various beam profiles for different spatial frequency spectra. First, we demonstrated high-precision slowly-varying intensity beam

profiles with an unprecedented high intensity accuracy. For flattop and linearly-tilted flattop beams, we achieved 0.20-0.34% root-mean-square (RMS) error over the entire measurement region. Second, two-dimensional sinusoidal-flattop beams were used to evaluate image precision versus system bandwidth. System evaluation confirmed that this system was capable of producing any spatial pattern with <3% RMS error for the most system bandwidth. This experiment extended the beam shaping to any system bandwidth and provided a reference to estimate the output image quality based on its spatial spectrum. Later experiment using a Lena-flattop beam profile demonstrated the arbitrary beam profile generation.

We implemented this system for applications on the homogenous optical lattice and dynamic optical trap generation. The DMD pattern was optimized by the iterative refinement process at the image feedback arm, and projected through a two-stage imaging system to form the desired beam profile at the working plane. Experiments demonstrated a high-precision beam shaping as well as a fast and dynamic control of the generated beam profile.

Table of Contents

List of Tables

List of Figures

Chapter 1 Introduction

1.1 MOTIVATION

Precise control of light beam profiles is important in many areas. For example, in some high-intensity laser systems [1], the beam profile is shaped to pre-compensate the spatial-dependent gain in the optical amplifier. In frequency response testing, spatial sinusoidal patterns are used to characterize the modulation transfer function (MTF) as a reliable evaluation tool of material, optical components, and electro-optical systems [2]. In addition, dynamic optical tweezers requires dot array or other complicated intensity profiles to trap biological cells or micro-particles [3]. Beam shaping techniques are also widely implemented in laser machining [4], 3-D profile measurement [5], and many other areas.

Our objective is design a beam shaping optical system to create a well-controlled laser beam to form the dynamic optical trap for ultracold atom experiments. Typically, an optical trap is formed by using tightly focused laser beams with a Gaussian profile [6] in two or three dimensions. Ultracold atoms are attracted to the intensity minima or maxima by the optical dipole force. However, the non-uniform intensity cross section of the Gaussian profile creates the inhomogeneous trap which limits the measurement area of the critical region between the Bose-Einstein condensate and the excited state [7].

Shaped laser beam profiles, on the other hand, have many advantages in this application. For example, a flattop beam profile creates a homogeneous optical trap and can lessen the undesirable effects of spatial inhomogeneities by creating an optical trap in which the potential well is of uniform depth. In addition, the effect of gravity on ultracold atoms can be compensated by a linearly-tilted flattop beam profile. Other beam profiles,

depending upon the specific use, are desirable to study local spectroscopy and critical boundaries between the various cold atom phases.

1.2 OBJECTIVES

Because ultra-cold atoms are sensitive to any intensity variation from the optical field, this system should be capable of generating arbitrary patterns with high intensity precision. For the homogenous optical potential, ultimate intensity flatness of the order of 0.1% root-mean-square error is desired. This requires the beam shaping system be capable of producing and measuring beam profiles with high accuracy. In the first step toward this goal, we want to get as close as we can by using an accurate initial measurement with refinement of the beam based on repeated measurements of the beam profile. In the future, one might consider further refinement by using the cold atom distribution, which is even more sensitive to small variations in the optical field.

In addition, it is desired to programmably control the generated pattern to dynamically modulate the shape of optical trap for the applications of ultracold atom physics, optical tweezers, and so on. We need a fairly good image precision (3-5%) while maintaining the required spatial resolution to display all the fine features in the target image.

As a result, the beam shaping system needs to meet the following design requirements. First, the generated pattern should have good intensity precision in conformity with the target image. We intend to use three steps to achieve this goal. As the first step, slowly-varying intensity profiles, such as the flattop and the linearly-tilted flattop beam, are designed to build the desired potential. Then, we choose 2-D sinusoidal-flattop beams as our target beam profiles to evaluate the performance of beam shaping.

System evaluation can be accomplished by examining the error level of sinusoidal-flattop patterns with different spatial periods. Finally, we can use this system evaluation result to predict the image precision for any given pattern and generate arbitrary patterns to programmably manipulate the shape of the optical trap.

Besides the objectives of generated beam profiles, we also have additional requirements regarding the beam shaping system. First, in order to be operated with other modules of the ultracold atoms experiment, it is necessary to shape the beam profile automatically with a fast operation speed. In addition, this system needs to have the ability to shape the incident beam profile from both coherent and incoherent light sources at different wavelengths to form a 3-D standing wave lattice [8] or a 2-D thin lattice [9] for different types of ultracold atom experiments. For each input wavelength, we can give up some degree of conversion efficiency in order to achieve high-precision beam shape control. Finally, the phase of the wave front is also important to establish a uniform optical standing wave field; a uniform, flat phase front over the flat-top region is required.

1.3 ORGANIZATION

This dissertation is organized as follows. Chapter 2 reviews related literature and proposes our method that overcomes shortcomings of previous beam shaping approaches. Chapter 3 discusses high-precision beam shaping concerns with a detailed analysis of ultimate beam shaping performance by using the proposed method.

Chapters 4 and 5 present various beam profiles generated by using this system according to the proposed steps. Chapter 4 presents slowly-varying intensity profile generation using various coherent and incoherent light sources at different wavelengths,

followed by a detailed analysis of energy efficiency and a brief discussion of system automation. Chapter 5 discusses beam shaping system evaluation using sinusoidal-flattop beam profiles. Arbitrary beam profile generation using an actual image will later confirm this system evaluation result. Chapters 6 and 7 describe two applications of this beam shaping system for the homogenous optical lattice (in Chapter 6) and the dynamic optical trap or laser tweezers (in Chapter 7). A summary concludes this dissertation in Chapter 8.

1.4 REFERENCES

[1] J. H. Kelly, L. J. Waxer, V. Bagnoud et al., "OMEGA EP: High-energy petawatt capability for the OMEGA laser facility," Journal De Physique. IV : JP. 133, 75-80.

[2] Sinusoidal MTF Optical Test Chart, Applied Image Inc., http://www.aig-imaging.com/Sinusoidal-MTF-Optical-Test-Chart.html, [Accessed at 2/6/2011].

[3] M. Montes-Usategui, E. Pleguezuelos, J. Andilla and E. Martín-Badosa, "Fast generation of holographic optical tweezers by random mask encoding of Fourier components," Opt. Express 14, 2101-2107 (2006).

[4] P. F. Van Kessel, L. J. Hornbeck, R. E. Meier, and M. R. Douglass, "A MEMS-based projection display," Proc. IEEE 86, 1687-1704 (1998).

[5] S. Zhang, and P. S. Huang, "High-resolution, real-time three-dimensional shape measurement", Opt. Eng. 45, 123601(2006).

[6] K.B. Davis, M.O. Mewes, M.R. Andrews, N.J. van Druten, D.S. Durfee, D.M. Kurn, and W. Ketterle "Bose–Einstein condensation in a gas of sodium atoms," Phys. Rev. Lett. 75 (22) (1995).

[7] N. Prokof'ev, O. Ruebenacker, and B. Svistunov, "Weakly interacting Bose gas in the vicinity of the normal-fluid–superfluid transition," Phys. Rev. A 69, 053625 (2004).

[8] J. K. Chin, D. E. Miller, Y. Liu, C. Stan, W. Setiawan, C. Sanner, K. Xu and W., Ketterle, "Evidence for superfluidity of ultracold fermions in an optical lattice,", Nature 443, 961-964 (2006).

[9] W. S. Bakr, J. I. Gillen, A. Peng, S. Fölling, and M. Greiner, "A quantum gas microscope for detecting single atoms in a Hubbard-regime optical lattice", Nature 462, 74-77 (2009).

Chapter 2 Method

In this chapter, we review literature about previous beam shaping approaches and analyze their shortcomings or disadvantages for our application. Then, we present our method for high-precision beam shaping. After the description of the optical layout and the introduction to the core device, we analyze the pattern design algorithm and the simulation result.

2.1 LITERATURE REVIEW

Laser beams with controlled intensity profiles can be generated through various approaches. Here, we briefly compare techniques that use transmissive optics (images of masks and masklike mirrors), refractive optics (lenses and aspheric elements), and diffractive optics (with propagation to a Fourier transform plane or to a near-field plane). Flattop beams are used as an example to compare the design results from these approaches.

Metal masks have been used in transmissive optical beam-shaping systems. Henesian *et al*. used binary metal pixels on a glass substrate for the National Ignition Facility [1] to optimize the performance of large-scale laser amplifiers [2]. Later work by Dorrer and Zuegel [3] demonstrated the error diffusion technique to design and simulate the performance of metal masks that formed flattop and other target beam profiles in an image plane following a low-pass filter. Although this approach can produce a desired beam that has a flat phase, it requires a known input intensity profile matched to the metal mask design. It is, of course, possible to make this technique adaptive by forming the mask by reflection from a binary-amplitude spatial light modulator (SLM). Our

design is derived from this method, and so it will be described in more detail later in this chapter.

Refractive optics is another approach for beam shaping [4,5]. The fundamental working procedure of this approach is to use an axicon lens and/or specially designed aspheric elements to redistribute and collimate input light to the desired pattern. For flattop beam generation, Hoffnagle and Jefferson [6] used a refractive optical system composed of two aspheric lenses to convert a collimated Gaussian beam into a flat-top beam. This method achieved 5% root-mean-square (RMS) intensity variation in a flat-top beam with 78% power conversion. The design has high power-conversion efficiency, is achromatic, and can achieve a flat output profile in both intensity and phase. Later work by Smilie and Suleski [7] used a refractive two-element system to convert the Gaussian irradiance into a flattop beam with various spot diameters by the lateral transition between the elements. Although this design introduced some freedom of output beam profiles, since the calculation of lens surfaces was based on specific input and output beam shapes, the whole system only work well for the limited input–output combinations. In addition, the technique can do nothing to reduce the effect of spatial noise and imperfections present in real laser beams.

The use of diffractive optics and holographic optical elements is popular for producing arbitrary light distributions. The conversion of Gaussian beams using diffractive optical elements (DOEs) has been intensively studied for many years. Both continuous phase elements [8,9] and annular phase plane elements containing two or more zones with binary phase value (usually 0 and π) [10,11] were proposed for beam shaping. However, since these DOEs can only be made for a specific output beam profiles, they, with other approaches of transmissive optics and refractive optics, do not

have any adaptive beam shaping ability. Thus, this intrinsic disadvantage limits the application of all these passive approaches.

As an active beam shaping technique, phase-only SLMs [12,13] have been used for beam shaping to achieve a design that is adaptable to arbitrary input and output beam shapes. Various algorithms, including iterative Fourier transform algorithms (IFTA) [14], simulated annealing (SA) algorithm [15], and generic algorithm [16], were applied to synthesize the refreshable hologram on the SLM for beam shaping. In a recent improvement to these techniques, Jesacher et al. [17] achieved complex amplitude modulation by encoding the spatial amplitude and phase distributions on different areas of the phase-only SLM. The input light was modulated sequentially and the target intensity pattern with desired phase front was reconstructed by a full Fourier transform.

For the design algorithm, Pasienski and DeMarco [18] reported a new IFTA to create the square cross-section, flat-top intensity profile. Their result pushed intensity error to an unimportant region of the output plane and reduced the error in the measurement region. In their adaptation of the IFTA, intensity was constrained only in the measurement region of the output plane, and phase was unconstrained. In a simulated result for an ideal phase-only SLM, they reported an RMS error of 1.5% with a power conversion efficiency of 45%. No data for the phase flatness were given. In general, such solutions are designed for a phase-only SLM and thus are inherently an approximation to ideal phase and amplitude modulation for the DOE. In addition, the reconstructed image generated by phase-only SLMs contains a zero-order diffraction beam (ZOD) from the non-modulated light [19]. Though many methods were proposed for ZOD suppression [20-22], it was difficult to completely eliminate this ZOD beam via a holographic approach [23]. Therefore, the imprecise beam shaping output from diffractive (holographic) optics excludes this approach for generating the dynamic optical trap.

One sees from this literature review that previous beam shaping approaches have various shortcomings or disadvantages in design flexibility and achievable intensity precision. Thus, it is necessary for us to design a novel beam shaping method to precisely control the output beam profile.

2.2 OPTICAL LAYOUT

For high-precision beam shaping, we constructed a test bench consisting of a laser, a digital micromirror device (DMD) SLM, and an imaging telescope with a spatial filter. The general layout of the test bench is shown in Fig. 2-1. The DMD (0.7XGA DDR DMD Discovery, Digital Light Innovation, Austin TX) has 1024 × 768 square pixels at a pitch of 13.68 μm. The input quasi-Gaussian beam from the light source is expanded and collimated with a 5× telescope to best fit the DMD size (14 mm × 10.5 mm). No effort was made to clean up this beam or to ensure that its profile was accurately Gaussian.

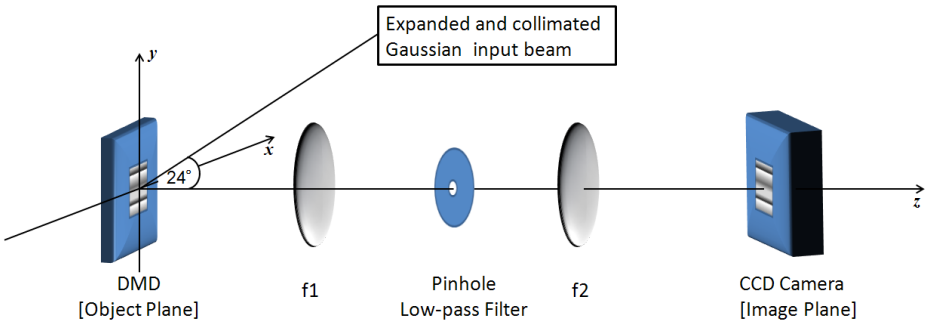

Figure 2-1: Optical layout of the DMD-based high-precision beam shaper.

The light reflected from this SLM passes through a 4f imaging system containing a pinhole that acts as a spatial-frequency low-pass filter. The output flat-top beam profile was measured at the output image plane of the telescope by a CCD camera. This image was sent to an algorithm that computed the binary reflectance function for the DMD. The specific pattern design process will be presented in detail later in this chapter.

To accurately measure the input and output beam profiles, we used the Scorpion SCOR-20SOM camera by Point Grey Research, Inc. that was prepared by Spiricon, Inc. to be windowless for accurate beam-profiling measurements with Spiricon laser beam diagnostic software. The Scorpion camera uses the Sony ICX274AL black and white CCD chip with 4.4 μm square pixels in a 1600 × 1200 array. The absence of the protective window minimizes fringes or diffraction patterns caused by parallel surfaces and dirty spots. The output beam profile was measured by using the same camera. Following this, an iterative process was used to refine the beam profile based on repeated accurate measurements of the output beam profile and adjustments to the binary DMD pixel pattern.

2.3 DMD OPERATION CONCERNS

As SLMs are now available with a wide range of specifications and modes of operation, some consideration is needed to select the correct one for high precision applications. For the beam shaping applications that we describe later, not only is precision required, but also time variation is not acceptable when an unchanging image is formed. This limits the SLM selection to one with a latched state that does not need refresh or polarity reversal as does a liquid crystal SLM. This requirement also excludes

the dither of pixel values at a high rate in order to achieve gray levels from a binary-amplitude SLM.

A short introduction to the DMD is given before the discussion of the pattern design. Texas Instruments (TI) Digital Micromirror Device (DMD) is an all-digital spatial light modulator with thousands of tiltable, fast-moving and addressable micromirrors (Figure 2-2(a)). As an all-digital spatial light modulator, the DMD is comprised of thousands of hinge-mounted microscopic mirrors (Figure 2-2(b)). A hidden yoke connects the hinge and supports the post. The hinge enables the mirror to rotate either $+\theta$ or $-\theta$ to realize the two binary states. Our experiment uses the DMD Discovery^{TM} series and has a rotation angle $\theta = \pm 12^{\circ}$. The micro-mechanical structure is mounted atop a SRAM cell. The CMOS addressing circuit controls the state of each mirror. A voltage can be applied to the either of two electrodes and exerts an electrostatic force which causes the mirror rotate quickly until the yoke contacts with the electrode. At this time, the mirror is electro-mechanically "latched" in its desired position. Thus the setting of one pixel is highly precise. What is required for grayscale image precision is a way to have a large number of pixels contribute to one resolution element of the projected image and yet have sufficient spatial resolution to form the image.

(a)

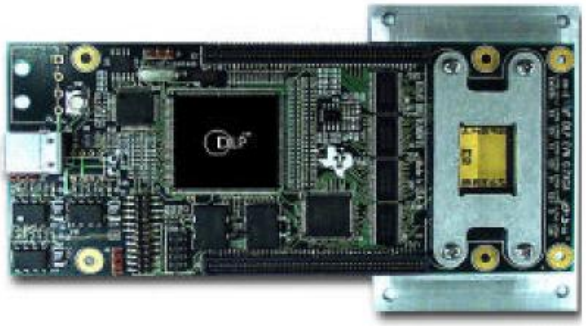

(b)

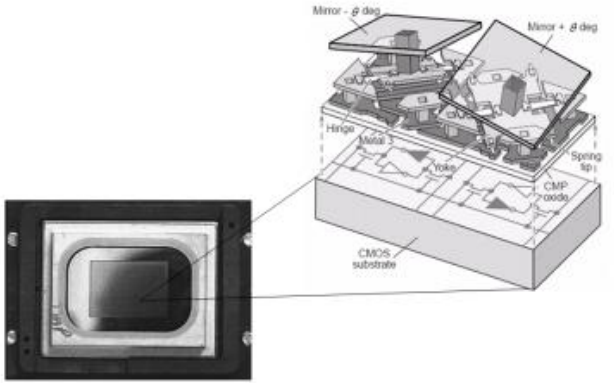

Figure 2-2: (a) DMD DiscoveryTM Controller Board with DMD and (b) Schematic of two DMD mirror pixels next to a typical DMD light modulator [24,25]

It is important to mention that the binary DMD pattern should stay unchanged during the beam shaping process because the ultracold atoms are sensitive to the intensity variation of the optical filed. This operation requirement of static pattern projection excludes the DLP display technology [26] based on the binary pulse modulation [27] for our application. If one would like to add programmed time variation of the formed image, it can be accomplished using the DMD by loading a series of images with as few as one or as many as all the pixels changed at frame rates up to 32 kHz. Slow and gradual variation from one image to another can be achieved using a sequence of images with small changes between each one. A frame rate of 32 kHz can be achieved through a direct digital interface to the DMD. For slower changes, we have achieved frame rates of 30-55 Hz using the USB interface to the DMD and loading a stack of pre-computed images.

2.4 DMD PATTERN DESIGN ALGORITHM

2.4.1 System operation

The way in which the desired beam profile is produced is based on binary DMD modulation plus imaging optics that includes a low-pass filter. The input Gaussian wave with the amplitude distribution $g_1(x,y)$ is incident on the DMD. The binary DMD pattern, $DMD(x,y)$, is determined by the measurement of the input beam and the target function. Thus, after the DMD, the amplitude distribution of the nth-order diffracted light (nearest the blaze angle), is given by

$$g_2(x,y)= g_1(x,y) \times DMD(x,y) \tag{2-1}$$

In the imaging telescope, the Fourier transform of the wave leaving the DMD surface is formed in the back focal plane of the first lens. A pinhole placed at this Fourier plane serves as a low-pass filter. The amplitude distribution in the frequency domain after the pinhole is given by

$$g_3(f_x,f_y)=F\{ g_2(x,y)\} \times h(f_x,f_y) \tag{2-2}$$

where $F\{ \}$ represents the Fourier transform operator and $h(f_x,f_y)$ is the binary-amplitude transmission of the pinhole. At the output plane, the light intensity distribution is the magnitude squared of the Fourier transform of $g_3(f_x,f_y)$. By proper control of the DMD pattern and the radius of the pinhole, the desired beam profile can be generated.

2.4.2 DMD pattern design

The binary DMD pattern is designed based on a two-step algorithm. Here, we use the flattop beam as the target function to illustrate this design process.

First, the input Gaussian is captured at the imaging plane. The target function is an eighth-order super-Lorentzian, *SL(x,y)*,whose width and height are referred to the input Gaussian and given by

$$G_1(x,y) = G_0 exp\left[-\frac{2r^2}{{r_G}^2}\right]$$
$$SL(x,y) = SL_0\left[1+\left|\frac{r}{r_{SL}}\right|^8\right]^{-1} \quad (2\text{-}3)$$

where $r = \sqrt{x^2+y^2}$ and relative parameters are chosen to be $r_{SL} = r_G/1.5$ and $SL_0 = 0.4G_0$. Based on the input Gaussian and target super-Lorentzian functions, the desired reflectance function is calculated by

$$R_1(x,y) = SL(x,y)/G_1(x,y) \quad (2\text{-}4)$$

This is illustrated in Fig. 2-3 for $r_G = N/3 = 256$ pixels and $r_{SL} = r_G/1.5$, where $N = 768$. These parameters give a target function that does not approach the Gaussian too closely, and the reflectance function does not become too sharply peaked or approach 1.0 (see Fig. 2-3). An increase in RMS error was observed when this limit was approached too closely.

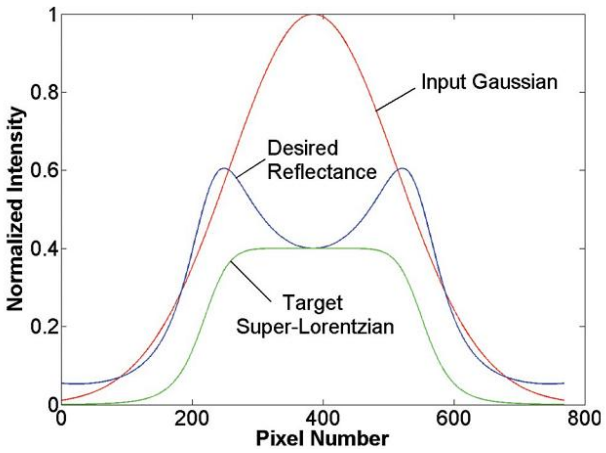

Figure 2-3: Cross sections of a simulated Gaussian input beam (r_G = 256 pixels), an eighth-order super-Lorentzian (SL) beam($r_{SL} = r_G / 1.5 = 171$ pixels), and the desired reflectance function, , to transform one into the other. The beam profiles and are defined in Eqs. (3) and (4).

Second, the multiplicative continuous amplitude reflectance, $r_1(x,y) = \sqrt{R_1(x,y)}$ is then processed by the error-diffusion algorithm [28] to produce the binary pixelated DMD pattern by rastering from left to right in a row and then from top to bottom in successive rows. Specifically, the binary value of *DMD(x,y)* is determined by comparing the desired amplitude reflectance $r_1(x,y)$ modified by the propagated errors from nearby pixels that have already been processed to the threshold value of 0.5. The error function is calculated by

$$e(x,y) = r_1(x,y) - DMD(x,y) \tag{2-5}$$

and the reflectance function is replaced by

$$r_1(x+a, y+b) = r_1(x+a, y+b) + c(a,b) \times e(x,y) \tag{2-6}$$

where *a* and *b* are row and column coordinate shifts of the nearest neighbor pixels yet to be processed. The weighting coefficients for the three nearest neighbors (*a = 1, b = 0; a = 1, b = 1; a = -1, b = 1*) depends upon the current reflectance $r_1(x, y)$. *c(a,b)* is the weighing factors of the error diffusion algorithm [28].

We simulated the performance of this beam shaping system by using a perfect Gaussian as the input and an eighth-order Super-Lorentzian as the target beam profile (eq. (3)). After reflection by the binary DMD pattern, the beam was passed though a simulated pinhole with an appropriate size that was chosen by a global search process. The RMS error of the simulated flattop was around 0.2% for a 180 pixel diameter disk centered on the flattop (see Fig. 2-3). We tried to generate the DMD pattern using several other methods, including a random dither algorithm and electronic screen methods, but neither performed as well as error diffusion without iterative correction.

In summary, previous beam shaping approaches are not capable of generating high-precision beam profile required in our application. On the other hand, the analysis and simulation illustrate that the proposed DMD-based beam shaping system is capable of high-precision performance and looks promising to satisfy our requirements. We will prove this by a detailed analysis of high-precision pattern generation and projection in the next chapter.

2.5 REFERENCES

[1] C. A. Haynam, P. J. Wegner, J. M. Auerbach, M. W. Bowers, S. N. Dixit, G. V. Erbert, G. M. Heestand, M. A. Henesian, M. R. Hermann, K. S. Jancaitis, K. R. Manes, C. D. Marshall, N. C. Mehta, J. Menapace, E. Moses, J. R. Murray, M. C. Nostrand, C. D. Orth, R. Patterson, R. A. Sacks, M. J. Shaw, M. Spaeth, S. B. Sutton, W. H. Williams,

C. C. Widmayer, R. K. White, S. T. Yang, and B. M. Van Wonterghem, "National Ignition Facility laser performance status," Appl. Opt. 46, 3276-3303 (2007).

[2] C. Dorrer, S. K.-H. Wei, P. Leung, M. Vargas, K. Wegman, J. Boulé, Z. Zhao, K. L. Marshall, and S. H. Chen, "High-damage-threshold static laser beam shaping using optically patterned liquid-crystal devices," Opt. Lett. 36, 4035-4037 (2011).

[3] C. Dorrer and J. D. Zuegel, "Design and analysis of binary beam shapers using error diffusion," J. Opt. Soc. Am. B 24, 1268–1275 (2007).

[4] D. Zeng, W. P. Latham and A. Kar, "Characteristic analysis of a refractive axicon system for optical trepanning", Opt. Eng. 45, 094302 (2006).

[5] A. Laskin and V. Laskin, "πShaper – Refractive Beam Shaping Optics for Advanced Laser Technologies" J. Phys.: Conf. Ser. 276 012171 (2011).

[6] J. A. Hoffnagle and C. M. Jefferson, "Design and performance of a refractive optical system that converts a Gaussian to a flattop beam," Appl. Opt. 39, 5488–5499 (2000).

[7] P. J. Smilie and T. J. Suleski, "Variable-diameter refractive beam shaping with freeform optical surfaces," Opt. Lett. 36, 4170-4172 (2011).

[8] J. Menapace, P. Davis, W. Steele, M. R. Hachkowski, A. Nelson, K. Xin, "MRF applications: on the road to making large-aperture ultraviolet laser resistant continuous phase plates for high-power lasers," Proc. SPIE 6403, 64030N (2006).

[9] C. C. Aleksoff, K. K. Ellis, and B. D. Neagle, "Holographic conversion of a Gaussian-beam to a near-field uniform beam," Opt. Eng. 30, 537–543 (1991).

[10]R. de Saint Denis, N. Passilly, M. Laroche, T. Mohammed-Brahim, and K. Ait-Ameur, "Beam-shaping longitudinal range of a binary diffractive optical element," Appl. Opt. 45, 8136–8141 (2006).

[11] J. Jia, C. Zhou, X. Sun, and L. Liu, "Superresolution laser beam shaping," Appl. Opt. 43, 2112–2117 (2004).

[12] T. Ando, Y. Ohtake, N. Matsumoto, T. Inoue, and N. Fukuchi, "Mode purities of Laguerre–Gaussian beams generated via complex-amplitude modulation using phase-only spatial light modulators," Opt. Lett. 34, 34-36 (2009).

[13] V. Bagnoud and J. D. Zuegel, "Independent phase and amplitude control of a laser beam by use of a single-phase-only spatial light modulator," Opt. Lett. 29, 295-297 (2004).

[14] J. S. Liu and M. R. Teghizadeh, "Iterative algorithm for the design of diffractive phase elements for lasr beam shaping", Opt. Letters 27 (16), 1463-1465 (2002).

[15] H. Ma, Z. Liu, X. Xu, X. Wang, Y. Ma and P. Zhou "Adaptive generation of a near-diffraction-limited square flattop beam with dual phase only liquid crystal spatial light modulators", J. Opt. 13 015707 (2011).

[16] A. Kostylev, A. Sobolev, T. Cherezova, and A. Kudryashov, "Genetic algorithm for intracavity laser beam shaping", Proc. SPIE 5876 587605 (2005).

[17] A. Jesacher, C. Maurer, A. Schwaighofer, S. Bernet, and M. Ritsch-Marte, "Near-perfect hologram reconstruction with a spatial light modulator," Opt. Express 16, 2597-2603 (2008).

[18] M. Pasienski and B. DeMarco, "A high-accuracy algorithm for designing arbitrary holographic atom traps," Opt. Express 16, 2176–2190 (2008).

[19] H. Zhang, J. Xie, J. Liu, and Y. Wang, "Elimination of a zero-order beam induced by a pixelated spatial light modulator for holographic projection," Applied Optics 48, 5834-5841 (2009).

[20] D. Palima and V. R. Daria, "Holographic projection of arbitrary light patterns with a suppressed zero-order beam," Applied Optics 46, 4197-4201 (2007).

[21] D. W. K. Wong and G. Chen, "Redistribution of the zero order by the use of a phase checkerboard pattern in computer generated holograms," Applied Optics 47, 602-610 (2008).

[22] J. Liang, Z. Cao, and M. F. Becker, "Phase Compression Technique to Suppress the Zero-Order Diffraction from a Pixelated Spatial Light Modulator (SLM)," [Frontiers in Optics, OSA Technical Digest (CD)], Optical Society of America, Washington DC, FThBB6 (2010).

[23] J. Liang, S. Wu, F. K. Fatemi, and M. F. Becker, "Suppression of the Zero-Order Diffracted Beam from a Pixelated Spatial Light Modulator by Phase Compression", submitted to Applied Optics (2012)

[24] "DMD Discovery™ 1100 Controller Board & Starter Kit," http://focus.ti.com/download/dlpdmd/25061976.pdf.

[25] L. J. Hornbeck, "Current Status and Future Applications for DMD™-Based Projection Displays," Proc. 5th Int'l Display Workshops, 1998.

[26] P.F. Van Kessel, L. J. Hornbeck, R. E. Meier, and M. R. Douglass, "A Mems-based Projection Display," Proc. IEEE, 86 1687 (1998).

[27] S. Sumriddetchkajorn, "Micromechanics-based digitally controlled tunable optical beam shaper," *Opt. Lett.* 28, 737-739 (2003).

[28] Ostromoukhov, V., "A simple and efficient error-diffusion algorithm," Proc. SIGGRAPH 2001, 567-572 (2001).

Chapter 3 Generating and projecting high-precision patterns

In this chapter, we discuss the beam shaping performance for different system bandwidths in theory. In the spatial domain, the system bandwidth determines the image precision and the spatial resolution of output images. This analysis leads to the iterative pattern refinement algorithm based on the point spread function (PSF). In the spatial frequency domain, high-precision beam shaping is realized by a well preserved image spectrum, which can be achieved by our method.

We shall demonstrate in theory that this beam shaping system is capable of producing the flattop beam profile as well as other profiles that satisfies the precision requirements for ultra-cold atom experiments as well as other applications.

3.1 IMAGE PRECISION IN THE SPATIAL DOMAIN

Shaping a laser beam or projecting an image with such a beam requires attention to both the required resolution for the pattern and the intensity precision since there are tradeoffs between these two quantities. In the spatial domain, one DMD pixel projects a PSF that describes the impulse response of the system (Fig. 3-1). The system bandwidth determined by the pinhole size controls the shape of the PSF, which represents the spatial resolution and image precision of the output image. For a given system bandwidth, the ultimate image accuracy is limited by the PSF peak, because one can never reach a smaller intensity variance than $\pm 1/2$ PSF peak amplitude by turning off or on a single DMD pixel. For smaller system bandwidth, a wider PSF with lower peak amplitude gives a higher image precision but a lower spatial resolution. On the other hand, larger system bandwidth produces a narrow PSF with large peak amplitude. This PSF reduces the image precision but gains high spatial resolution. For a given system bandwidth,

changing the state of one DMD pixel adds or subtracts one PSF amplitude at the output plane. Thus, the system shows the best-possible performance when the output image reaches $\pm 1/2$ PSF in amplitude error variance for the given bandwidth.

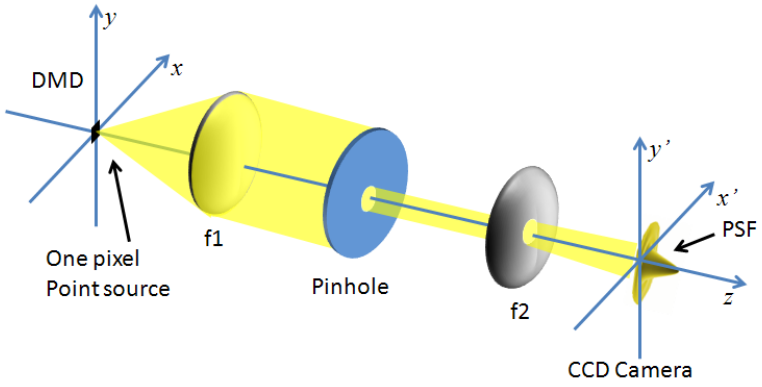

Figure 3-1: Impulse response of the DMD-based high-precision beam shaper

As a result, we can regard the output image as the superposition of PSFs at different locations. Because turning on or off one DMD pixel adds or subtracts one PSF at the corresponding location, we can use PSF as a non-orthogonal basis set for image feedback to improve the image quality of the output beam profile. We will describe the image feedback process in detail in the Section 3.2.

The theoretical limit of this system can be determined by backward propagating one image resolution point at the image plane to the DMD plane. Because of the limited system bandwidth, this point source forms a back projected PSF at the DMD plane (Fig. 3-2). The consideration is the size of the back projected PSF with respect to the DMD pixel spacing because all DMD pixels underneath this PSF contribute to the amplitude of the image point at the image plane. Because the irradiance is derived from the setting of several adjacent pixels, the intensity can be set with greater precision. This is particularly advantageous for the case of a binary-amplitude SLM such as the DLP device. If the

resolution of a wide PSF is sufficient for image production, then hundreds of pixels can contribute to the illumination of one image point. This also means the image precision is limited by the digitization error because the minimal incremental step is one DMD pixel.

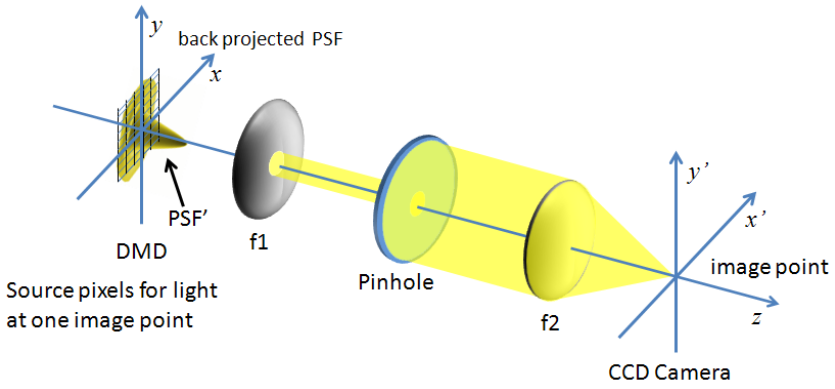

Figure 3-2: Backward projected PSF to determine the theoretical limit of the DMD-based beam shaping system.

Mathematically, the theoretical limit is equivalent to $\pm 1/2$ PSF variation at the image plane and is found by estimating the number of binary DMD pixels that contribute to the intensity at an output point. Equivalently, this is the number of pixels within the PSF expressed at the DMD face. The digitization error, σ_{DE}, is defined by $\sigma_{DE} = \frac{1}{\sqrt{12}\times MSB}$, where MSB stands for most significant bit and can be calculated by $MSB = A_{eff}/A_p$ where Ap and Aeff are the areas of the DMD pixel and the effective area of the PSF main lobe, respectively. Because PSF does not have a spatial uniform profile, the DMD pixels at the edge of the PSF contributes less intensity than the DMD pixels at the center of PSF. Thus, we used a unit-height cylinder to define the effective main lobe. This unit-height cylinder having the effective PSF radius has precisely the same volume as the main lobe of the PSF. The radius of the effective PSF area is very

close to its HWHM radius. As a result, in terms of the normalized system bandwidth, R_N, the digitization noise becomes

$$\sigma_{DE} = \frac{\pi}{\sqrt{12}} \times \left(\frac{R_N}{c}\right)^2 \tag{3-1}$$

where c = 1.830 is the effective PSF radius described above in coordinates normalized to the maximum system bandwidth, which is calculated by f_{max} = (2×DMD pixel pitch)$^{-1}$. The calculated digitization error for different system bandwidth is shown in Fig. 3-3. One sees that the digitization error is 0.08% for the normalized system bandwidth f = 1/18.9, corresponding to the major spatial spectrum of a flattop beam. This result proves that the DMD-based beam shaping system has ability to generate the 0.1% RMS flattop beam in theory.

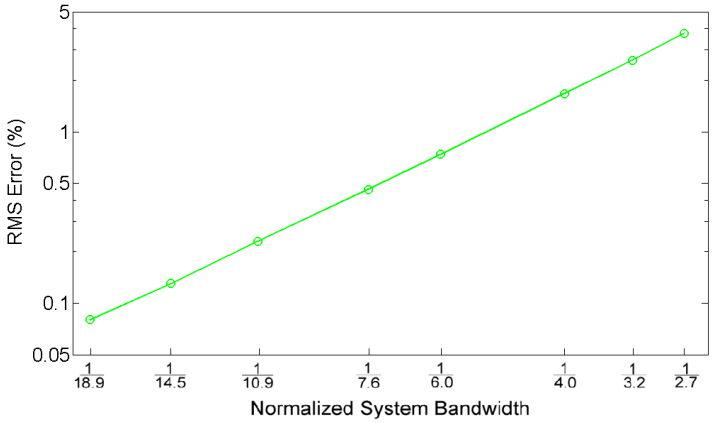

Figure 3-3: Digitization error versus normalized system bandwidth

3.2 PSF-BASED ITERATIVE PATTERN REFINEMENT

Based on the above analysis, we proposed PSF-based iterative refinement that consists of the following steps (Fig. 3-4(a)). First, the PSF is calculated based on the

system bandwidth and is used in the iterative refinement process. The calculated PSF is compared with the measured PSF at the output plane. This comparison is used to check the system alignment because a misaligned pinhole produces an asymmetric PSF. As a blazed diffraction grating with certain pixel pitch, locations of diffraction orders are determined by the incident angle and the wavelength while the energy distribution (sinc center) is determined by the tilting angle of DMD pixels. As a result, when one DMD pixel is turned on for the PSF measurement, all the "OFF" pixels produce a weak diffraction over that overlaps with the light from the "ON" pixel. The interference of these two parts of light changes the shape of the actual PSF. Fortunately, our measurement shows that the amplitude peak of an actual PSF is quite close to the calculated result (Fig. 3-4 (b)). For this reason, we used the calculated PSF for iterative pattern refinement.

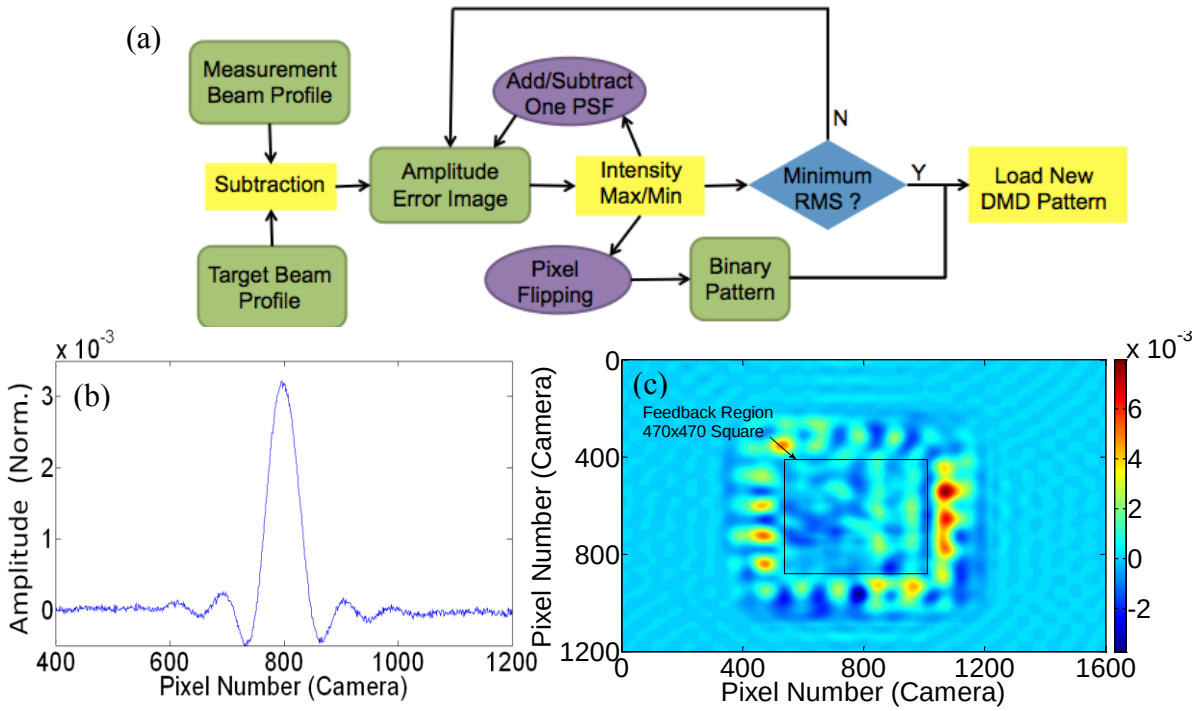

Figure 3-5: PSF-based iterative pattern refinement. (a) Flow chart, (b) measured PSF, and (c) amplitude error image of a flattop beam.

Second, a camera image, after applying a digital low-pass filter (LPF) (see Section 3.5 for details) to remove speckle, is subtracted from the target image to obtain the amplitude error image (Fig. 3-4 (c)). For the selected image feedback region, an inner loop suppresses intensity peaks and lifts the intensity valleys in the amplitude error image. This loop operates on one peak-valley pair per iteration. For each iteration, maximum and minimum intensities are found, and corresponding locations on the DMD are determined. Then, one PSF is subtracted (for an intensity maximum) or added (for an intensity minimum) at these two locations on the amplitude error image. The PSF amplitude at these locations is spatially modulated by the input Gaussian beam function. These two DMD pixels are flipped and the RMS error is recomputed without taking a new camera image. Another peak and valley are corrected in the same way until the inner loop terminates when the RMS error reaches its minimum. Finally, the refined pattern is loaded into the DMD, and the camera captures another output image. We repeat the second step for this new camera image, and the entire feedback process ends when the RMS error stops decreasing.

3.3 IMAGE PRECISION IN THE SPATIAL FREQUENCY DOMAIN

The preceding analysis can also be viewed in the spatial frequency domain to reach the same conclusion by asking the question, "how precisely is the image spectrum recovered?" Required resolution is clearly defined by the spectral width of the target image that must be passed by the modulation transfer function (MTF) of the optical system. Since the width of the MTF is inversely proportional to the width of the PSF, the wide PSF case is represented by a narrow MTF. Thus the spectral content of the image must fit within the system MTF. For such a bandwidth-limited optical system, the pixel

spatial frequency can be considerably higher than the highest frequency within the system MTF. The excess SLM bandwidth is utilized to increase the amplitude precision of the low frequency components of the spectrum within the required MTF.

The case of an optical system with a circularly symmetric low pass filter is illustrated in Fig. 3-5 that uses an example of the power spectrum of an 8th-order super-Lorentzian laser beam, i.e., a flattop beam with smoothly tapered edges and somewhat low spatial frequency content. The fidelity of the beam profile can be maintained with a low pass filter that cuts the spectrum at -30 to -40 dB below the peak. This same concept will be used later to illustrate the noise reduction treatment of camera images of similar beams and patterns.

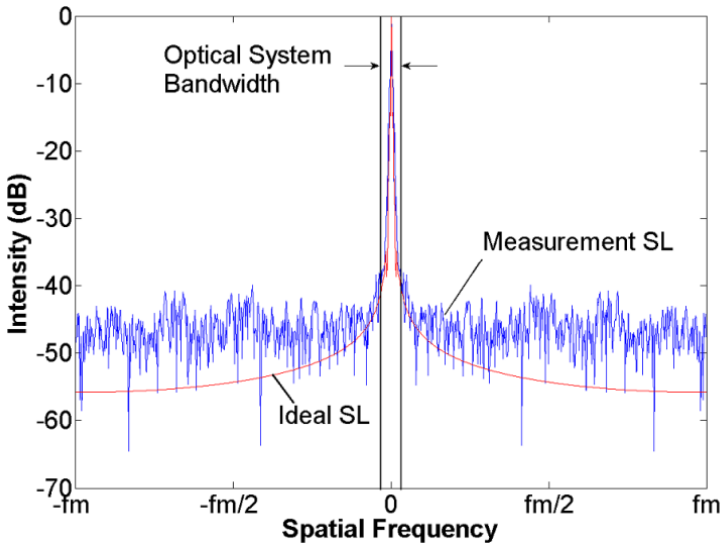

Figure 3-5: Cross section of the spatial frequency spectrum of the camera image of an 8th-order super-Lorentzian (SL) flattop laser beam indicating the optical system bandwidth needed to precisely represent the beam profile. The measured and ideal spectra are superposed. The maximum spatial frequency for the 4.4 μm camera pixel pitch is shown as *fm*.

3.4 ERROR DIFFUSION ALGORITHM

When the error diffusion algorithm is used to design the binary DMD pattern, the spatial-frequency spectrum of light from the DMD consists of the target image spectrum plus a high-pass filtered error spectrum [1]. The high-pass filter, induced from the error diffusion algorithm, possesses "blue noise" characteristics in the spatial frequency domain by achieving a quasi-random distribution of the binary values. The "blue-noise" brings small distortion at the low and middle spatial frequencies and large error at high frequencies as shown in Fig. 3-6. This indicates that this technique is suited to design band-limited target images.

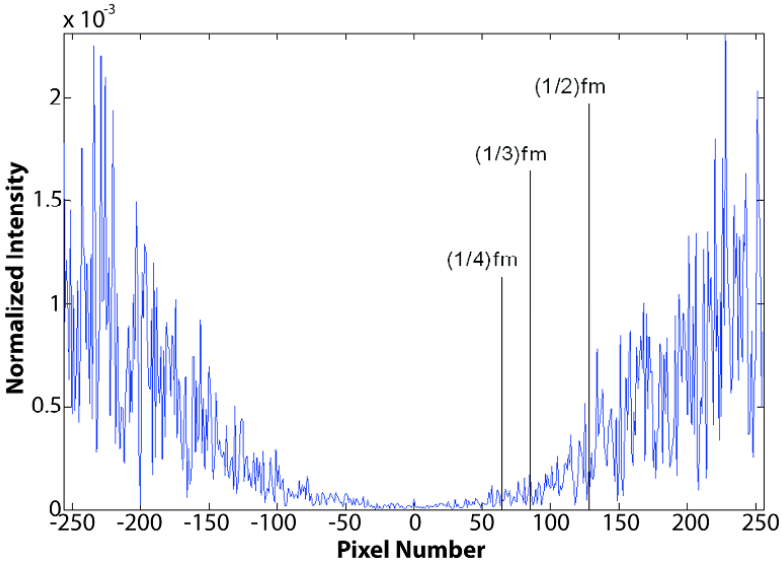

Figure 3-6: Simulated spatial frequency spectrum of the output of the beam shaping system when the target profile is set to a constant gray reflectance of 80% using our error diffusion algorithm. The DC term is blocked for this display.

The adjustable pinhole serves as a low-pass filter to control the optical bandwidth. As a result, most high-frequency noise in the blue-noise spectrum is filtered out, leaving the well-preserved original target image spectrum. Since major frequency components for most images are within 1/3 to 1/2 of the maximal spatial frequency [2], it is expected that

this system is capable of generating various high-precision spatial patterns for different system bandwidths.

3.5 DIGITAL LOW-PASS FILTER DESIGN

Although the system bandwidth is limited by the pinhole, the coherent speckle caused by light scattering between camera pixels induced additional high spatial-frequency noise. In order to separate the error introduced by the optical system from that introduced by coherent speckle and camera noise, a digital low pass filter (LPF) with an equivalent cutoff frequency to the pinhole in the experiment was applied to camera images. The spatial frequencies that were eliminated by the digital LPF were more than 35 dB below the peak of the spectrum. Thus the major frequency components of the beam profile were not affected. The remaining error after the digital LPF comes from design algorithm imperfections, residual low-frequency spatial gain noise in the camera, quantization error due to the finite number of DMD pixels that form one resolution element, and photon noise (in decreasing order of size). A detailed error analysis will be given in the next Chapter.

3.6 SUMMARY

As a summary, we present several concerns for high-precision pattern generation and projection. In the spatial domain, the output image is subject to the tradeoff between image precision and spatial resolution that is controlled by the PSF. PSF-based iterative pattern refinement is proposed to improve the image quality. The ultimate precision of the refinement process is limited by the digitization error, which is below 0.1% for the flattop beam spectrum and remains less than 5% for most of the system bandwidth. In the

spatial frequency domain, the spectrum of the target image needs to be precisely preserved to achieve high-precision beam shaping. The blue-noise spectrum produced by the error diffusion algorithm only induces little noise to the low and middle frequency content while the noisy high-frequency band is filtered out by the pinhole low-pass filter. Analysis from both domains illustrates that the DMD-based beam shaping system can generate and project high-precision patterns for ultracold atom experiments and other applications.

3.7 REFERENCES

[1] K. Knox, "Error image in error diffusion", Proc. SPIE 1657, 268-279 (1992).

[2] M. F. Becker, J. Liang, R. N. Kohn Jr. and D. J. Heinzen, “High-precision laser beam shaping using binary-amplitude DLP spatial light modulators,” Proc. SPIE 7596, 75960A (2010).

Chapter 4 Slowly-varying intensity beam profile generation

In this chapter, we present high-precision beam shaping for slowly-varying intensity beam profile generation [1-3]. The major target image is a flattop beam (and a linearly-tilted flattop beam). The DMD pattern is first generated by the error diffusion algorithm and then optimized by the PSF-based iterative pattern refinement. Several coherent and incoherent light sources at different wavelengths were used in beam shaping experiments to compare the image precision. A detailed analysis of energy conversion efficiency illustrates that the diffraction efficiency plays an important role to determine the overall system energy efficiency. Finally, LabVIEW-based system automation is introduced for fast and automated beam shaping control.

4.1 SLOWLY-VARYING INTENSITY BEAM SHAPING

4.1.1 He-Ne laser

The experiment was first conducted using a 633 nm He-Ne laser. For this wavelength, the DMD imaging telescope had a magnification of -5/6 and used 300 mm and 250 mm focal length lenses for f1 and f2, respectively. The pinhole diameter was 610 μm.

To demonstrate the flexibility of the system, we implemented circular and square eighth-order super-Lorentzian profiles at 633 nm. In this case, the raw camera image was used for the iterative refinement process without low-pass filtering. The RMS flatness for the first-generation circular flattop beam and the beam after the fifth refinement iteration (Table 4-1) is calculated by

$$RMS = \sqrt{\frac{1}{N} \sum_{(x,y) \in MA} \left(\frac{I_{Out}(x,y)}{I_{Tar}(x,y)} - 1 \right)^2} \qquad (4\text{-}1)$$

where $I_{Out}(x,y)$ and $I_{Tar}(x,y)$ are the intensity of the output image and target image with equalized image power, and N is the total number of pixels in the measurement area (MA).

Refinement reduced the RMS error from 1.5% to 1.0%. After the digital low-pass filter, the error was reduced to 0.67% RMS over the flattop region. Fig. 4-1 displays horizontal cross sections through the highest peak and lowest valley of the circular flattop beam without refinement superimposed on the same cross sections after five refinement iterations. As shown in the figure, the operation of the refinement algorithm successfully adjusts the peaks and valleys adaptively.

Table 4-1: Measured RMS error for the initial flattop beam and after the fifth refinement iteration versus diameter for a circular flattop beam at 633 nm wavelength.

Dia. (pixel)		64	126	196	286	310	324 [a]
Dia. (mm)		0.28	0.55	0.86	1.26	1.36	1.43
RMS	Initial	1.0	1.1	1.2	1.3	1.4	1.5
Error	5 Iterations	0.93	0.90	0.93	0.96	1.00	1.06
(%)	LPF [b]	0.61	0.52	0.57	0.60	0.67	0.77

[a] The diameter of 324 pixels (1.43 mm) is slightly outside the flattop boundary.

[b] After digital LPF at 1/32 of the maximum spatial frequency.

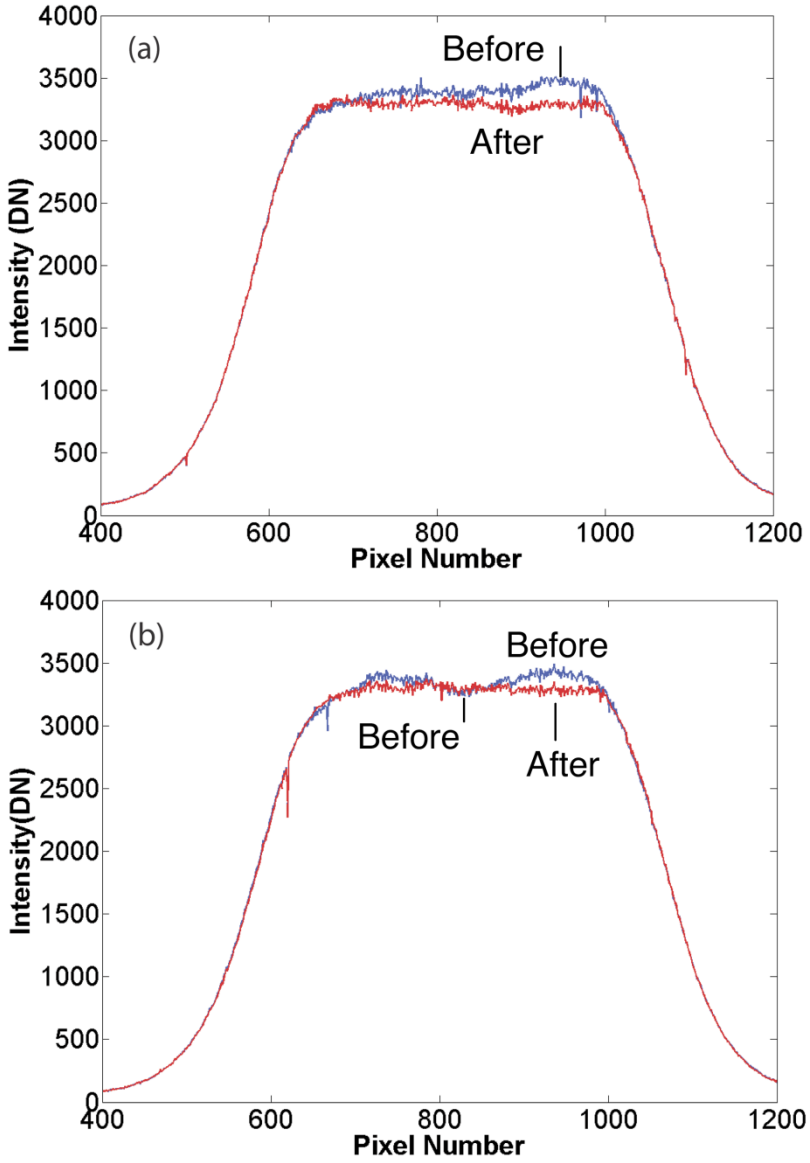

Figure 4-1: Cross sections of the flattop beam before and after the iterative refinement process: through the highest peak (a), and through the lowest valley (b).

The square flattop beam experiment yielded similar results for RMS error as shown in Table 4-2. The RMS error was 0.9% over the 1.39 mm square flattop region.

When digitally low-pass filtered, the error was reduced to 0.61% RMS for the same region. A camera image of the resulting square beam is shown in Fig. 4-2.

Table 4-2: Measured RMS error for the square flattop versus width for 633 nm wavelength.

Square width (pixel)		30	50	100	160	200	240 [a]
Square width (mm)		0.13	0.22	0.44	0.70	0.88	1.06
RMS Error (%)	Initial	0.96	1.00	1.10	1.20	1.39	1.73
	5 iterations	0.81	0.89	0.89	0.86	0.90	1.19
	LPF [b]	0.48	0.55	0.61	0.56	0.61	1.00

[a] The width of 240 pixels (1.06 mm) is slightly outside the flattop boundary.

[b] After digital LPF at 1/32 of the maximum spatial frequency.

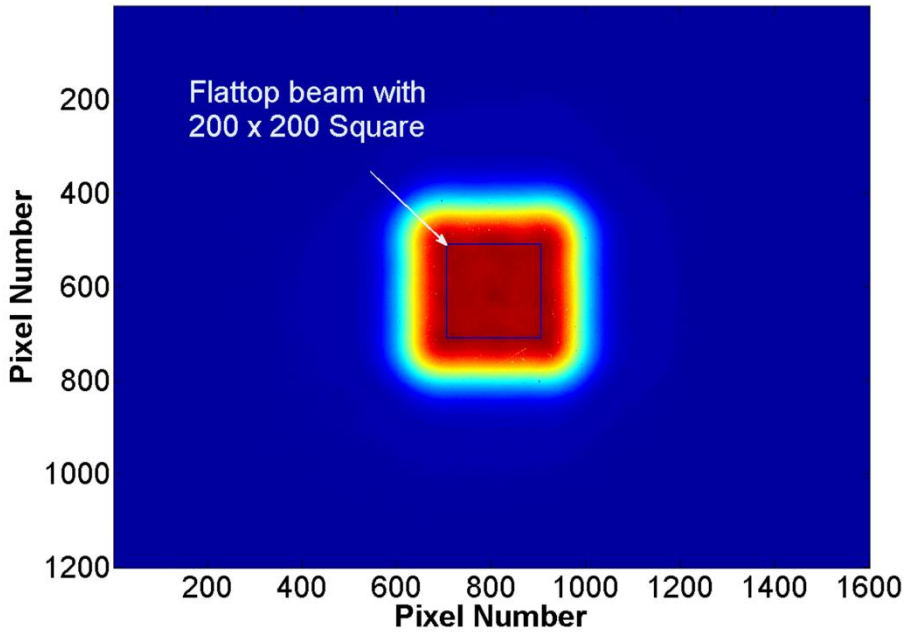

Figure 4-2: Camera image of the square flattop beam.

4.1.2 Fiber laser

We used a fiber laser oscillator from NP Photonics for beam shaping at 1064 nm. The imaging telescope magnification was changed to −4:5, and the two lenses were focal lengths of 500 and 400 mm. The pinhole diameter was changed to 1.2 mm. The magnification change was made to accommodate the slightly larger beam diameter incident on the DMD, and the pinhole was changed to accommodate both the changed beam size and the new wavelength.

The experiment achieved 1.12% RMS flatness after refinement of the circular flattop region. The sizes of the regions with noise below a specified level are shown in Fig. 4-3. The RMS error of the raw image and the digitally low-pass filtered image are given in Table 4-3. It is notable that the RMS error across the whole flattop was reduced to 0.23%.

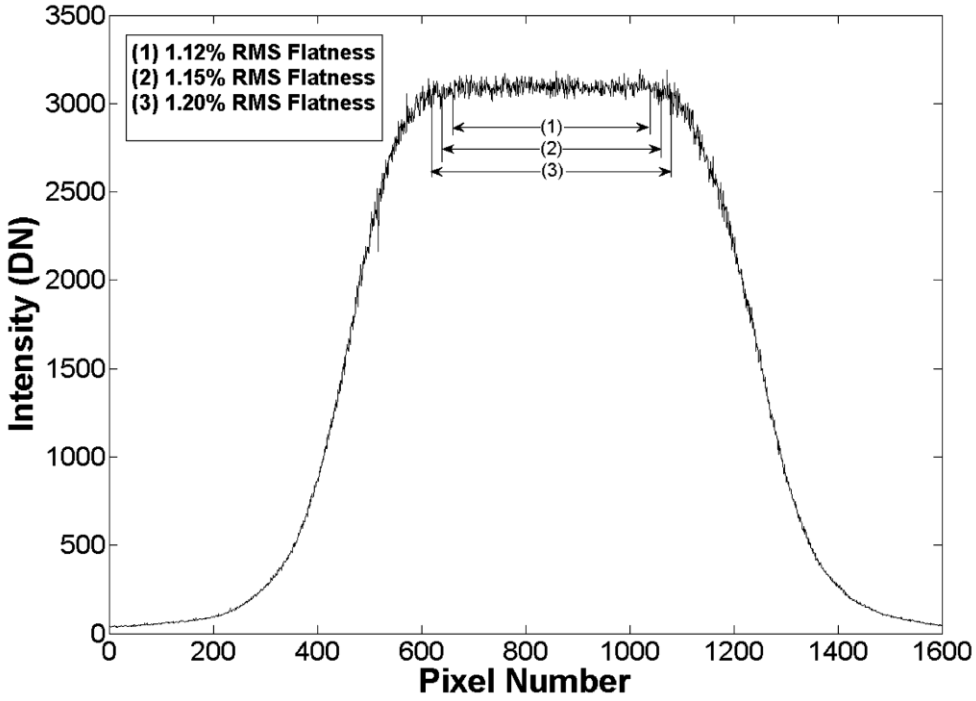

Figure 4-3: Horizontal cross section of the flattop beam (1064 nm) after 17 refinement iterations. Arrows indicate the diameter within which the error is below the indicated level.

Table 4-3: Measured RMS error for the initial circular flattop beam and after 17 refinement iterations versus diameter at 1064 nm wavelength.

Dia. (pixel)		52	120	230	340	376	422[a]
Dia. (mm)		0.23	0.53	1.01	1.50	1.65	1.86
RMS	Initial	1.70	1.60	1.50	1.60	1.70	1.80
error	17 Iterations	1.08	1.13	1.11	1.12	1.12	1.15
(%)	1/96 LPF[b]	0.17	0.30	0.25	0.23	0.23	0.24

[a] The diameter of 422 pixels (1.86 mm) is slightly outside the flattop boundary.

[b] The radius of the digital LPF is 1/96 of the maximum spatial frequency.

Table 4-4 summarizes the RMS error data the over the entire flat-top region for all the tabulated experiments, with and without the digital LPF, and at both 633 and 1064 nm. Although the improved refinement process used for the 1064 nm experiments decreased the RMS error in the digitally filtered image by a significant factor, the unfiltered result was similar for both cases. This indicates that other noise sources at high spatial frequency (e.g., coherent interference and speckle noise) dominate the uniformity of the light intensity in the raw camera image.

Table 4-4: Summary of RMS error in the whole flattop beam area for three cases studied.

Flattop case	RMS error after feedback	RMS error after digital LPF [a]
circle (dia.=310 pixel) 633 nm	1.00	0.67
square (width=200 pixel) 633 nm	0.90	0.61
circle (dia.=376 pixel) 1064 nm	1.12	0.23

[a] The radius of the digital LPF is 1/32 and 1/96 of the maximum spatial frequency for the 633 nm and 1064 nm measurements, respectively.

An additional experiment was conducted to produce a beam profile that was a linearly tilted flattop that will be useful for gravity compensation in the ultracold atom experiments described in Chapter 1. Both circular and square cross-section, tilted flattop beams were implemented with similar performance. A sample image of the square cross-section beam is shown in Fig. 4-4. This experimental result had 1.19% RMS error in the raw camera image and 0.45% RMS error after applying the digital LPF.

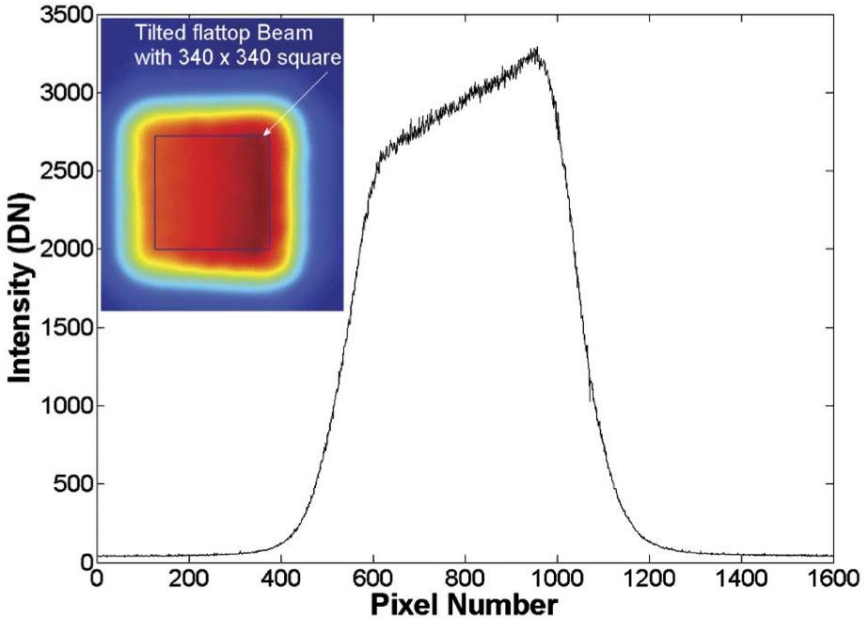

Figure 4-4: Cross section and top view (inset) of the square tilted flattop beam.

4.1.3 Laser diode (LD)

The narrower-bandwidth, low-coherence source, a 781 nm SMF-pigtailed laser diode (LPS-785-FC, Thorlabs) replaced the SLED for the second set of experiments. An 800 μm pinhole was found to be the optimum spatial filter. This was smaller than for the SLED since the measured bandwidth of the laser diode was 1.3 nm, corresponding to 336 μm lateral displacement along the diagonal at the Fourier plane.

The experiment achieved 0.88% RMS flatness after refinement in a raw camera image. After digital low-pass filtering, the RMS error was reduced to 0.20% over the entire flattop beam (dia. = 1.32 mm). The cross sections of the raw image and the digitally low-pass filtered image are compared in Fig. 4-5 and their RMS errors with different flattop region sizes are given in Table 4-5.

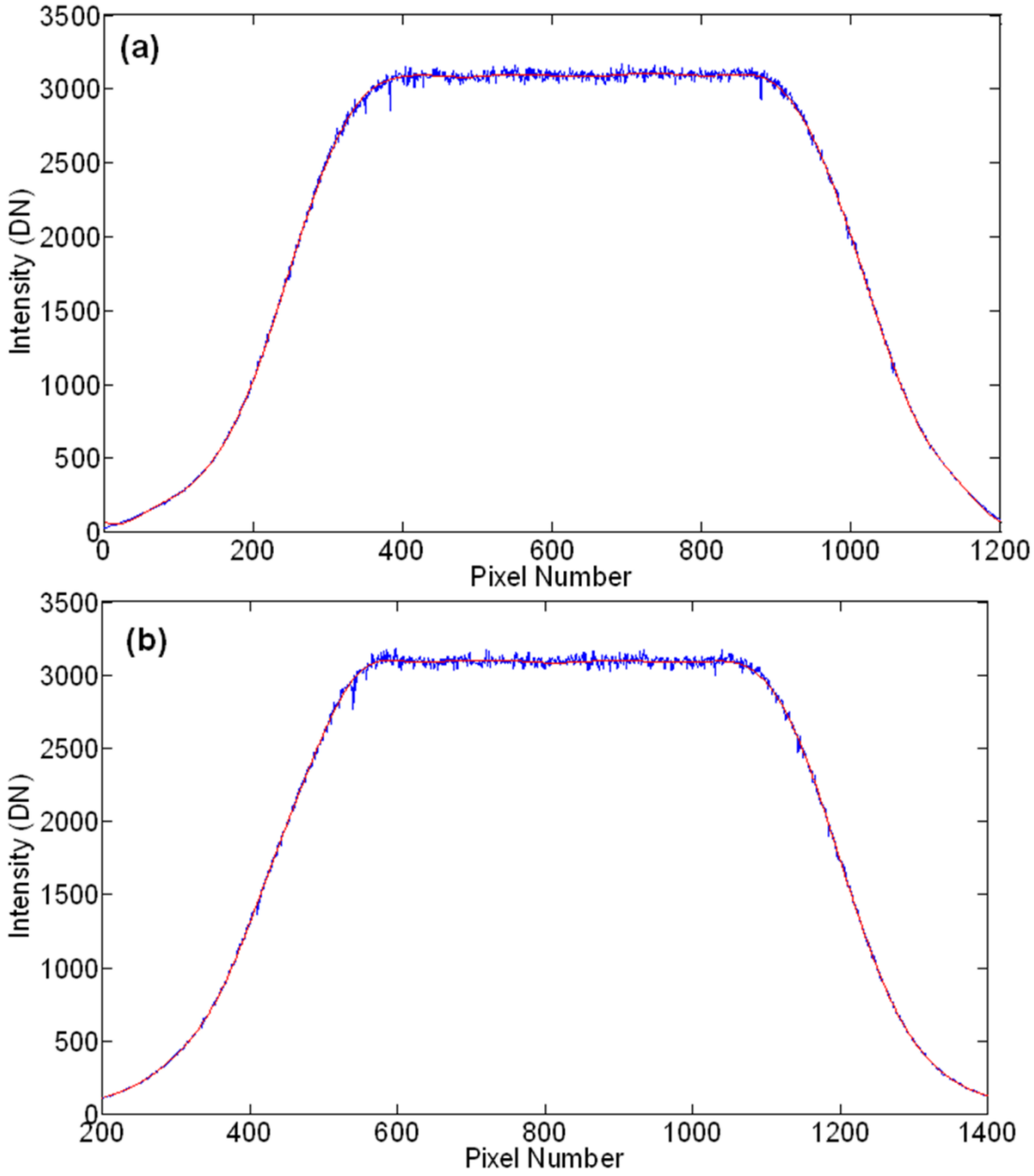

Figure 4-5: Vertical (a) and horizontal (b) cross sections of the raw image (blue) and the digital LPF image (red).

Table 4-5: Measured RMS error for the flattop beam versus diameter using a 781 nm laser diode.

Diameter (pixel)		60	100	160	200	240	300	360[a]
Diameter (mm)		0.26	0.44	0.70	0.88	1.06	1.32	1.58
RMS Error (%)	20 Iterations	0.87	0.88	0.89	0.89	0.89	0.88	0.88
	LPF[b]	0.21	0.16	0.19	0.19	0.18	0.20	0.22

[a] The diameter of 360 pixels (1.58 mm) is slightly out of flattop region.

[b] Cutoff frequency at 1/90 of maximum spatial frequency.

4.1.4 Super-luminescent Light Emission Diode (SLD)

The incoherent light source was a SMF-pigtailed SLED centered at 760 nm (EXS7505-8411, EXALOS). The pinhole diameter was 1.0 mm for the best beam shaping performance. Refinement was iterated 20 times while reducing the scale of the peaks and valleys that were treated. The camera image of the final flattop beam is shown in Fig. 4-6. Table 4-6 summarizes the RMS flatness of the raw camera image for different diameters over the central region. The RMS error over the entire flattop area (diameter = 300 pixels) was 0.81%. After the digital LPF, this error was reduced to 0.26%.

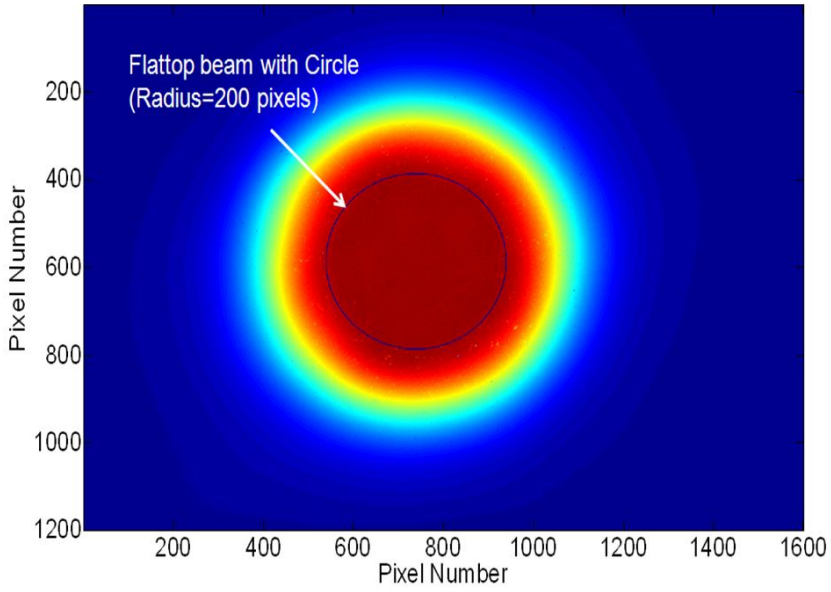

Figure 4-6: Camera image of the circular flattop beam using the 760 nm SLED.

Table 4-6: Measured RMS error for the flattop beam versus diameter using the 760 nm SLED.

Diameter (pixel)		60	100	160	200	240	300	360[a]
Diameter (mm)		0.26	0.44	0.70	0.88	1.06	1.32	1.58
RMS	20 Iterations	0.80	0.80	0.82	0.81	0.82	0.81	0.83
Error (%)	LPF[b]	0.10	0.16	0.17	0.18	0.20	0.26	1.32

[a] The diameter of 360 pixels (1.58 mm) is slightly out of the flattop region.

[b] Cutoff frequency at 1/71 of maximum spatial frequency.

Note that the RMS error from diameter 240 to 360 pixels increased significantly after applying the 1/71 digital LPF. Since the SLED is based on amplified spontaneous emission without any optical cavity feedback, it has a wide spectral bandwidth of 22 nm

(FWHM) centered at 760 nm (25°C). Since the input light is incident at 45° to DMD face, diffraction displaces different wavelengths laterally along the diagonal direction. Therefore, only a small portion of light passes through the pinhole at the back focal plane of the first lens. This also caused a non-uniform spatial filtering where more spatial frequency content was cutoff in one diagonal direction than the other. As a result, the output flattop beam had a slightly elliptical shape (tilted at 45°) at the image plane (Fig. 4-6). This slight ellipticity is mainly visible only at the lowest intensity contours of the beam profile, not at the central flattop region. In addition, the digital LPF increased this non-uniform spatial modulation when applied to the output image, and thus caused the rapid increase of RMS error for larger diameters. Finally, spatial filtering led to severe energy loss since the pinhole excluded wavelengths outside of a bandwidth of ~2 nm.

4.1.5 Comparison of results

In order to compare the results for all of the various laser sources, the data for RMS error have been gathered in Table 4-7. The table compares the RMS error over the entire flattop region for all four light sources, with and without the digital LPF. For the raw image, it is clear that coherent light sources produced more RMS error from speckle in the camera image. The 1064 nm SMF laser, which has the highest coherence, has the largest intensity variance. On the other hand, both low-coherence light sources generated less than 0.9% RMS error, and the 760 nm SLED had the best intensity flatness and also the lowest coherence.

Table 4-7: Summary of RMS error in the whole flattop beam area for coherent and incoherent light sources.

Light sources		Coherent		Incoherent	
		633 nm He-Ne laser	1064 nm SMF laser	760 nm SLED	781 nm Laser diode
Flattop diameter (mm)		1.36	1.50	1.32	1.32
Digital LPF[a]		1/32	1/96	1/71	1/90
RMS Error (%)	Raw Image	1.00	1.12	0.81	0.88
	LPF	0.67	0.23	0.26	0.20

[a] The radius of the digital LPF represents as the fraction of the maximum spatial frequency.

The RMS error decreased significantly after applying the digital LPF, illustrating that high spatial frequencies dominated the error in the raw camera image. The data for the 633 nm He-Ne laser was excluded from this analysis because the optical system was modified by changing the lens focal length, pinhole size, and radius of digital LPF. In addition, this data was obtained after only 5 refinement iterations compared to 17 iterations for 1064 nm and 20 iterations for the SLED and laser diode. Thus, we expect more intensity variation in the output beam for the He-Ne laser experiment. For the other three light sources, we obtained similar RMS errors, ranging from 0.20-0.26%.

4.1.6 Error analysis

As part of the DMD pattern design algorithm, the propagation of the measured input beam profile reflected from the DMD face and passed through the spatial filter optical system is simulated. The iterative refinement routine is run to convergence in

order to obtain the initial DMD pixel pattern. In the iterative refinement, DMD pixels corresponding to the intensity peak or valley in the simulated output beam are flipped until no further reduction of RMS error is obtained. For these simulations (run with 1064 nm beam parameters), the minimum RMS error oscillated between 0.19% and 0.31% as the flattop level was adjusted from 33 to 45% of the peak of the input Gaussian beam. This illustrates the range of RMS error in the flattop due to bit setting errors in the DMD pattern-generating algorithm.

Next, consider the resolution available with a finite number of binary DMD pixels. In the major lobe of the point-spread function (PSF) of the pinhole low pass filter, there are about 610 pixels at the DMD plane. The least significant bit (LSB) is 1/610 or 0.16%. If represented as a digitizer of slightly over 9 bits, the RMS error of the digitization process would be 0.29 LSB = 0.05% RMS. This leaves only a little room for improving the simulated performance of the DMD design algorithm to reach this minimum.

Compare these simulations with the experimental results after the digital low-pass filter (LPF); the lowest RMS error was 0.20% (Table 4-7), and other measured values ranged up to 0.35%. The camera noise consists of photon noise that is 0.02% RMS before the digital LPF and is deemed negligible after this filter. Spatial gain noise is estimated to be around 0.1% RMS after the LPF, based on white frame measurements. The digital LPF has achieved the goal of eliminating much of the photon noise, spatial gain noise, and speckle noise from the flattop image without removing spatial frequency content that passed through the pinhole spatial filter.

After subtracting the spatial gain noise power, the remaining experimental RMS error ranges from 0.20 to 0.34% RMS. This is in agreement with the results from the simulation for the residual RMS error in the flattop beam (0.19 to 0.31%). For the

number of DMD pixels contained within the flattop beam, the RMS error may only be suppressed to around 0.1 to 0.2%. Although illuminating more DMD pixels would result in a smaller LSB and better performance from the iterative optimization routines, this would also illuminate the more curved portion of the DMD face and introduce more astigmatism and phase nonuniformity in the beam. If the beam diameter were increased by 1.4 times, the number of pixels would double and thus the expected RMS error would decrease by ½. We conclude that at a measured RMS error of 0.23% we are very near the ultimate performance possible of around 0.1% RMS error.

4.2 ENERGY CONVERSION EFFICIENCY

From experiments using various light sources, we observed that the energy conversion efficiency of the DMD-based beam shaper depends on the operation wavelength. The energy conversion efficiency depends on DMD mirror reflectivity, antireflection coating transmission of its window, DMD fill factor, diffraction efficiency (depending on DMD mirror pitch and tilt angle, and the wavelength), and the user-selected loss in converting the input quasi-Gaussian to a flattop (typically 40% efficiency). For wavelengths that we used in the experiments, the first three factors stay the same (as does the Gaussian-to-flattop conversion percentage) while the diffraction efficiency varies for each individual wavelength.

Each DMD pixel is latched by the hinge at a 45° diagonal direction. In our system configuration, the input light is incident in this diagonal plane so that the reflected (or diffracted) beam can exit perpendicular to the DMD surface (Fig. 4-7 (a)). As a result, we choose two diagonal directions as the coordinates to establish the model to calculate DMD diffraction efficiency (Fig. 4-7 (b)).

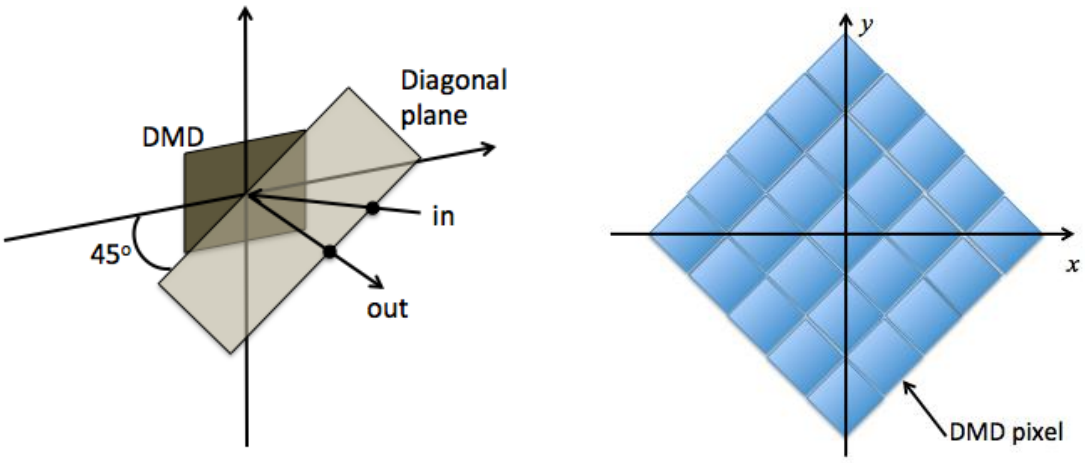

(a) (b)

Figure 4-7: (a) DMD input beam geometry (b) DMD diffraction model.

Plane wave incidents at angle a to the DMD surface normal (linear phase with respect to the in- plane dimension x in this case). Each DMD pixel is tilted at an angle b with respect to the surface (its surface normal is b with respect to the DMD surface normal). Under the paraxial approximation, the proper mathematical description of the DMD array for the tilted wave incident is,

$$u(x,y) = exp\left(\frac{j2\pi ax}{\lambda}\right) \times \left\{\left[exp\left(\frac{j4\pi bx}{\lambda}\right) \times Rect\left(\frac{1}{w}\left(\frac{x}{\sqrt{2}}+\frac{y}{\sqrt{2}}\right), \frac{1}{w}\left(\frac{x}{\sqrt{2}}-\frac{y}{\sqrt{2}}\right)\right)\right]\right\} \otimes comb\left(\frac{1}{p}\left(\frac{x}{\sqrt{2}}+\frac{y}{\sqrt{2}}\right), \frac{1}{p}\left(\frac{x}{\sqrt{2}}-\frac{y}{\sqrt{2}}\right)\right) \quad (4\text{-}2)$$

where *w* and *p* are the width and pitch of a DMD pixel. The first exponential function is the tilted wave phase and the second exponential function is the DMD pixel surface tilt. The "Rect" function defines square DMD pixels that are 45° rotated from the *x*-*y* coordinates.

In order to calculate the Fourier transform of the "Rect" and "comb" functions, we define *x'-y'* coordinates which is 45° rotated from the x-y coordinate. The relation between these two coordinate systems is $x' = \frac{\sqrt{2}}{2}(x+y)$ and $y' = \frac{\sqrt{2}}{2}(x-y)$. In the *x'-y'* coordinates, the Fourier transforms of the "rect" and "comb" function provide $F\left\{\mathrm{Rect}\left(\frac{x'}{w}, \frac{y'}{w}\right)\right\} = w^2 \mathrm{sinc}(wf_x', wf_y')$ and $F\left\{\mathrm{comb}\left(\frac{x'}{w}, \frac{y'}{w}\right)\right\} = \frac{1}{p^2}\mathrm{comb}(pf_x', pf_y')$. By using the same coordinate transform in the spatial frequency domain, we get $f_x = \frac{\sqrt{2}}{2}(f_x' - f_y')$ and $f_y = \frac{\sqrt{2}}{2}(f_x' + f_y')$. Therefore, we get

$$\begin{cases} F\left\{Rect\left(\frac{1}{w}\left(\frac{x}{\sqrt{2}}+\frac{y}{\sqrt{2}}\right), \frac{1}{w}\left(\frac{x}{\sqrt{2}}-\frac{y}{\sqrt{2}}\right)\right)\right\} = w^2 sinc\left(\frac{w}{\sqrt{2}}(f_x+f_y), \frac{w}{\sqrt{2}}(f_x-f_y)\right) & (4\text{-}3) \\ F\left\{comb\left(\frac{1}{p}\left(\frac{x}{\sqrt{2}}+\frac{y}{\sqrt{2}}\right), \frac{1}{p}\left(\frac{x}{\sqrt{2}}-\frac{y}{\sqrt{2}}\right)\right)\right\} = \frac{1}{p^2} comb\left(\frac{p}{\sqrt{2}}(f_x+f_y), \frac{p}{\sqrt{2}}(f_x-f_y)\right) & (4\text{-}4) \end{cases}$$

Use (4-3), (4-4), and the frequency shift theorem, the Fourier transform of Eq. (4-2) is given by

$$U(f_x, f_y) = \left(\frac{w}{p}\right)^2 F\left\{exp\left(\frac{j2\pi a x}{\lambda}\right)\right\} \otimes \left\{\left[sinc\left(\frac{w}{\sqrt{2}}\left(f_x - \frac{2b}{\lambda} + f_y\right), \frac{w}{\sqrt{2}}\left(f_x - \frac{2b}{\lambda} - f_y\right)\right)\right] \times comb\left(\frac{p}{\sqrt{2}}(f_x+f_y), \frac{p}{\sqrt{2}}(f_x-f_y)\right)\right\}$$

$$= \left(\frac{w}{p}\right)^2 \left[sinc\left(\frac{w}{\sqrt{2}}\left(f_x - \frac{2b+a}{\lambda} + f_y\right), \frac{w}{\sqrt{2}}\left(f_x - \frac{2b+a}{\lambda} - f_y\right)\right)\right] \times comb\left(\frac{p}{\sqrt{2}}\left(f_x - \frac{a}{\lambda} + f_y\right), \frac{p}{\sqrt{2}}\left(f_x - \frac{a}{\lambda} - f_y\right)\right) \quad (4\text{-}4)$$

Based on Eq. (4-4), the center of sinc in the Fourier transform follows the law of reflection and stays at the angle $\theta_{sinc} = 2b+a$. The center order (zero order) from the comb function is always centered at the angle of specular reflection, $\theta_0 = a$. Thus, the angular difference between the sinc center and the zero order is always $\Delta\theta = 2b$ (twice as

the DMD pixel tilting angle). This means for the arbitrary incidence angle within a small range, the samples of the comb remain fixed on the sinc pattern.

Because the input light is only x dependent, we can simplify Eq. (4-4) to

$$U_x(f_x, f_y) = (\frac{w}{p})^2 sinc^2\left(\frac{w}{\sqrt{2}}\left(f_x - \frac{2b+a}{\lambda}\right)\right) \times comb\left(\frac{p}{\sqrt{2}}\left(f_x - \frac{a}{\lambda}\right)\right) \quad (4\text{-}5)$$

Equation (4-5) illustrates the amplitude diffraction distribution along the fx axis. The diffraction angle of the mth order can be calculated by $\theta_m = \frac{\sqrt{2}m\lambda}{p} + a$. By ignoring the area fill factor $(\frac{w}{p})^2$, the energy diffraction efficiency is therefore given by

$$\eta_m = sinc^4\left(\frac{w}{\sqrt{2}}\left(\frac{\sqrt{2}m}{p} - \frac{2b}{\lambda}\right)\right) \quad (4\text{-}6)$$

It is clear for eq. (4-6) that the energy diffraction efficiency only depends on the operation wavelength for a certain diffraction order.

We simulated the diffraction efficiency for the .7" XGA DMD with pixel width *w = 12.68 μm*, pixel pitch *p = 13.68 μm*, and the tilting angle *b = 12°*. The simulation result is plotted in Fig. 4-8. The diffraction efficiency is 53% for 1064 nm (4th order) and 73% for 633 nm (6th order). For the 781 nm laser diode, the diffraction efficiency increased drastically to nearly 100% (5th order at 781 nm). Taking into account the loss from DMD device itself [4] and the Gaussian-flattop conversion loss, the resulting overall conversion efficiency at 781 nm was calculated to be 21.2%. The measured result for 781 nm was 19.8%; almost three times larger than the 7% conversion measured at 1064 nm.

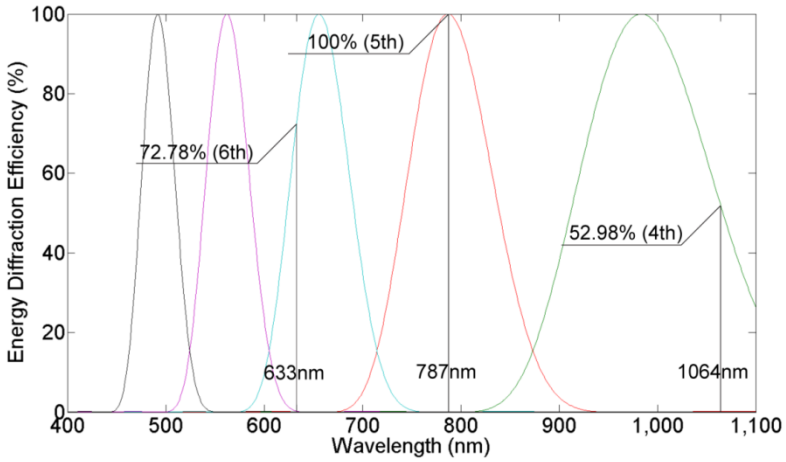

Figure 4-8: .7" XGA DMD energy diffraction efficiency at visible and NIR wavelength ranges.

If one wanted to maximize the conversion efficiency at 1064 nm for example, the DMD pixel pitch and window antireflection coatings need to be optimized. The pitch of the .55 XGA DLP chip of 10.8 μm has its 3rd order diffraction peak very close to 1064 nm. Unfortunately, this device is currently available with only visible AR coatings. So, either a custom window must be designed, or the IR window (from the other DLP chip configurations) would be used to replace the original window, but with a less-than-optimum total transmission of 78%.

4.3 LabVIEW PROGRAM DESIGN

The automation of the system will now be described. The LabVIEW based system was used for and greatly accelerated data acquisition in the experiments with the low-coherence sources [3]. Two similar user interfaces are used: first to obtain the initial DMD pattern and initial flattop beam, and second to control the iterative refinement of the beam. As an example, the first user interface is shown in Fig. 4-9. The required input parameters for both interfaces are shown in Table 4-9. The automation program

integrates image acquisition (Spiricon Laser Beam Profiler software), target-profile generation and refinement (Matlab), and DMD pattern loading (Discovery 1100 or 4000 DMD boards and drivers). Before running the automated routine, users need to complete camera calibration tasks: dark field subtraction, white field measurement, system alignment, and scaling factor measurement (camera pixels to DMD pixels).

The LabVIEW automated program was successfully implemented with the DMD-based beam shaping system and used to accelerate these experiments. To reach the first flattop beam took 57 seconds, and to perform the iterative refinement took an additional 71 seconds.

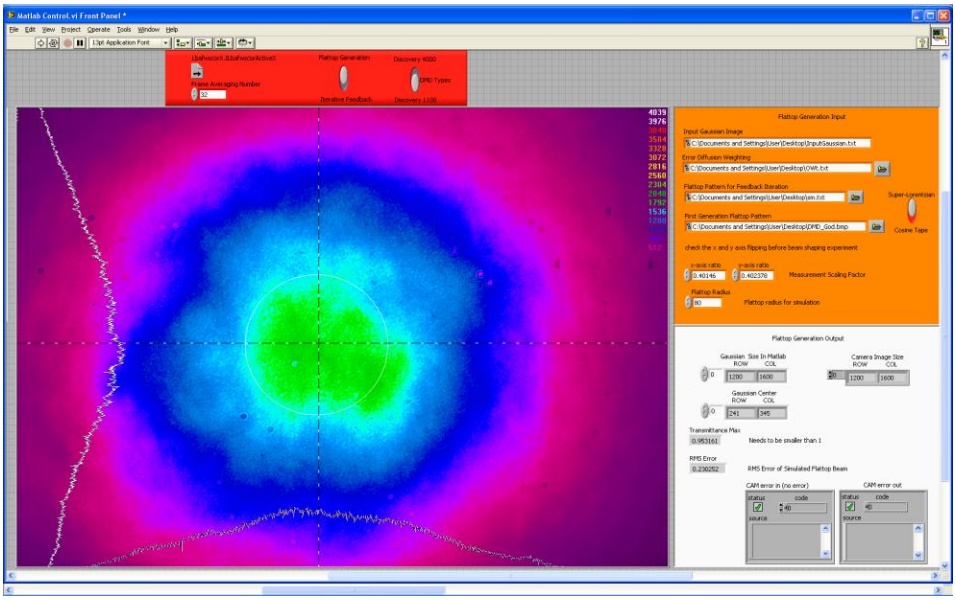

Figure 4-9: Example user interface of LabVIEW automated beam shaper for flattop generation. Illustrated is a typical quasi-Gaussian beam profile from SLED that is input to the system.

Table 4-8: Input parameters for LabVIEW automated beam shaper

Flattop generation	Iterative refinement
Number of frames to average	Number of frames to average
DMD type	DMD flattop pattern
Target function dimensions	Number of iterations
Error diffusion weights	Digital LPF radius
DMD pattern storage address	DMD pattern storage address

4.3 SUMMARY

As a summary, we demonstrated slowly-varying intensity beam profile generation using the DMD-based high-precision beam shaper. The generated flattop beams and other profiles have 0.20-0.34% intensity RMS error. The noise analysis showed that most of residual noise came from the pattern design error. The image precision is close to the 0.1% RMS error objective. The energy efficiency analysis demonstrated that the diffraction efficiency for the DMD was optimized at certain blaze wavelengths. Finally, LabVIEW-based automation increased the operation speed of the pattern generation and iterative feedback process and made data collection quite straightforward.

4.4 REFERENCES

[1] J. Liang, R. N. Kohn Jr., M. F. Becker and D. J. Heinzen, "1.5% root-mean-square flat-intensity laser beam formed using a binary-amplitude spatial light modulator," Appl. Opt. 48, 1955-1962 (2009).

[2] J. Liang, R. N. Kohn Jr., M. F. Becker and D. J. Heinzen, "High-precision laser beam shaping using a binary-amplitude spatial light modulator," Appl. Opt. 49, 1323-1330 (2010).

[3] J. Liang, R. N. Kohn Jr., M. F. Becker and D. J. Heinzen, "High-precision beam shaper for coherent and incoherent light using a DLP spatial light modulator", Proc. SPIE 7932, 793208 (2011).

[4] DMD 0.7 XGA 12º DDR DMD Discovery™ Datasheet, http://focus.ti.com/download/dlpdmd/2503686.pdf, access on [1/31/2012]

Chapter 5 Arbitrary beam profile generation

So far, we have demonstrated high-precision slowly-varying beam profile generation. All these beam profiles have narrow system bandwidths because they do not have many fine features in the image. This chapter extends high-precision beam shaping to arbitrary profiles. We will first evaluate the system spatial frequency response and characterize output image precision with respect to the system bandwidth [1]. Then, we will test system performance using a real picture to verify the system evaluation.

5.1 SYSTEM EVALUATION

5.1.1 Sinusoidal-flattop beam

Spatial sinusoids are commonly used as test patterns for a wide variety of applications. Based on their spatial periodicity, applications of sinusoidal beam profiles include 3-D shape measurement [2], quality control and defect detection [3], nonlinear structured-illumination microscopy [4] and non-invasive imaging in biomedical engineering[5]. Based on their single-frequency characteristic, sinusoidal patterns are also powerful tools to test frequency response in system evaluation [6,7] and to provide a spatial carrier frequency for optical signal processing [8].

As the first step toward arbitrary beam shaping generation, we choose a two dimensional (2-D) sinusoidal-flattop beam as our target beam profile to evaluate the performance of beam shaping. A sinusoidal-flattop beam is defined as a flattop beam that is embedded with a 2-D sinusoidal pattern. These target images produce different sinusoidal beam profiles in the flattop region. In addition, since the flattop beam profile has a narrow spatial spectrum, the sinusoidal flattop beams maintain the single-frequency characteristics as pure sinusoids and enable us to investigate beam-shaping performance

versus bandwidth. Evaluation of our beam shaping system can be accomplished by examining the error level of sinusoidal-flattop patterns with different spatial periods.

5.1.2 Experimental Conditions

A series of sinusoidal-flattop beams with different spatial periods were generated for the purpose of system performance evaluation. We used a 781 nm SMF-pigtailed laser diode (LPF-785-FC, Thorlabs) as the light source to achieve high energy-conversion efficiency. The two lenses in the telescope were chosen as 500 mm and 400 mm focal lengths to give a -4/5 magnification. A flattop with a cosine taper function, *CP(x,y)*, was chosen as the flattop beam. The sinusoidal-flattop profile, *SF(x,y)*, is formed by

$$SF(x,y) = \left[A\sin\left(\frac{2\pi x}{P}\right)+1\right]\left[B\sin\left(\frac{2\pi y}{P}\right)+1\right] CP(x,y) \qquad (5\text{-}1)$$

where P is the spatial period of the sinusoidal-flattop profile. Sinusoidal amplitude A and B are chosen to be $A = B = 0.2$ in the experiment. A .7" XGA DMD (Discovery 1100 with 13.68 μm pixel pitch) was used in the beam shaping experiment. The first-generation DMD pattern was designed by the error diffusion algorithm starting with the measured input quasi-Gaussian to achieve the target sinusoidal-flattop profile. The optimized pinhole diameter was determined by a global search algorithm in a numerical simulation and varied from 1.5 mm to 71 mm for different system bandwidths. We set the feedback region to be a 190×190 pixel square (2.6 mm × 2.6 mm) at the DMD plane because the central part contains all major pattern information. PSF-based iterative pattern refinement was conducted for 7 to 20 times for RMS error to reach a minimum for the different sinusoid periods.

The quality of sinusoidal-flattop generation was examined by the intensity RMS error percentage between the output beam profile and the original target image. The total image power (sum of pixel intensities) in the measurement area of 400×400 pixels (1.76 mm × 1.76 mm) at the image plane was equalized to that of the target image. The RMS error is calculated by Eq. (4-1).

5.1.2 Experimental Results

Experimental results demonstrated that the DMD-based beam shaper successfully generated various sinusoidal-flattop beam profiles. Figure 5-1 shows measurement results for a typical series of sinusoidal-flattop beams of different sinusoid periods and a pure flattop beam as a reference. As the sinusoidal period decreased from ∞ (no sinusoid) to 6 DMD pixels, we observed increasing intensity error in the measured beam profile. The RMS error increased from 0.95% to 11.87% for a raw camera image, illustrating that increasing the system bandwidth reduced image accuracy. The RMS error after the digital LPF showed the same trend, increasing from 0.19% to 12.08%. High-precision images were obtained for low system bandwidth. A detailed analysis of the RMS error is given in the following sections.

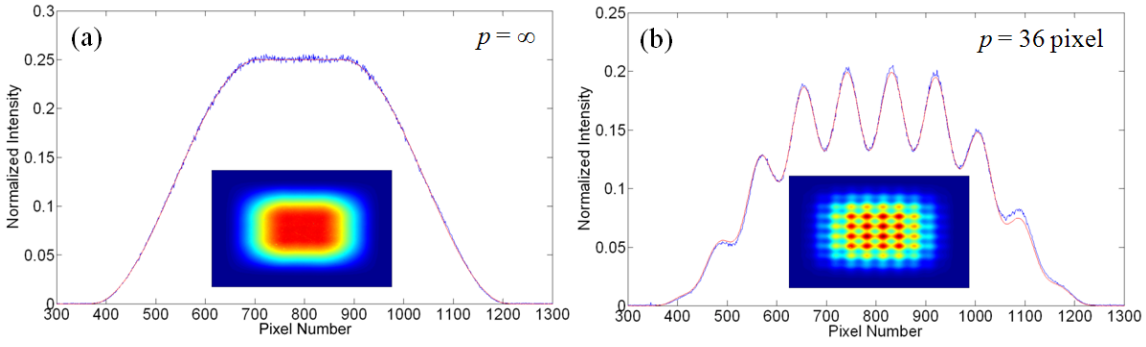

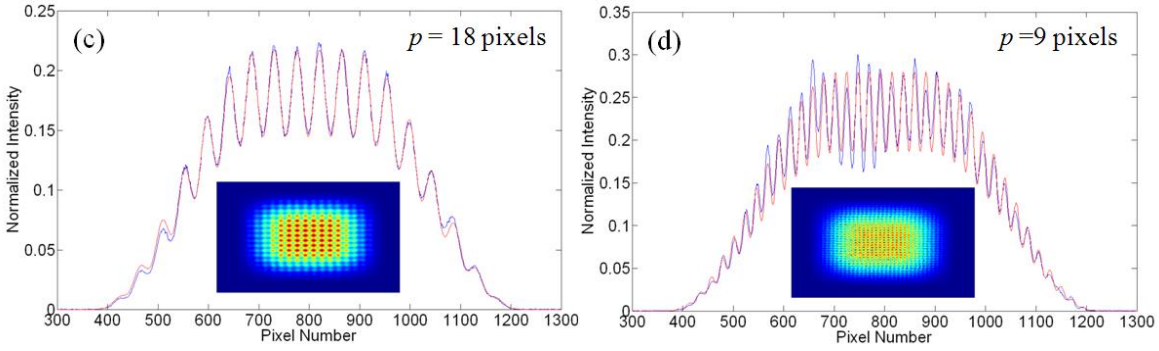

Figure 5-1: Top view (inset) and horizontal cross sections of the raw image (red) and the target image (blue) of sinusoidal-flattop beam profile with different spatial periods.

5.1.3 System Evaluation

The intensity RMS error of the series of sinusoidal-flattop beams is used as the criterion to evaluate system performance for different system bandwidths to explicitly illustrate the impact of spatial filtering. The system bandwidth is calculated based on the pinhole radii for the sinusoidal-flattop beam series and normalized by the maximal system bandwidth (f_m = (2 ×DMD pixel pitch) $^{-1}$ = 36.6 mm^{-1}).

Three types of intensity RMS error are examined for each sinusoidal-flattop beam profile. First, the RMS error of raw camera images after iterative pattern refinement directly represents the beam profile quality from experimental measurement. Second, the error of digitally low-pass-filtered experimental results estimates actual optical beam quality. Finally, we also analyze the simulated sinusoidal-flattop beam profile to examine error in the designed pattern produced by the error diffusion algorithm.

All calculation results are summarized in Table 5-1. The system bandwidth is slightly larger than the spatial carrier frequency of the sinusoidal pattern because of the finite spatial extent of the flattop pattern. The system is capable of producing high-

precision patterns with around 1% RMS error for system bandwidth below $1/10.9$ (*period* = 36 DMD pixels). The RMS error gradually increases but stays below 3% until the bandwidth reaches $1/4.0$ (*period* = 12 DMD pixels). The image accuracy decreases significantly beyond this to around 10% RMS error for $1/2.7$ system bandwidth (*period* = 6 DMD pixels).

Table 5-1: Summary of RMS error for sinusoidal-flattop beam profiles

Sinusoidal Period (DMD pixels)		N/A	48	36	24	18	12	9	6
Normalized System Bandwidth		1/18.9	1/14.5	1/10.9	1/7.6	1/6.0	1/4.0	1/3.2	1/2.7
RMS Error (%)	Simulated	0.51	0.62	0.89	1.23	1.86	3.08	6.45	10.89
	Raw Image	0.95	1.03	1.32	1.68	1.98	2.93	7.58	11.87
	Digital LPF Image	0.19	0.38	0.85	1.40	1.65	2.75	7.73	12.08

5.1.4 Noise analysis

We compare the three types of RMS error presented in Section 5.1.3 with respect to the digitization error calculated in Chapter 3 (Figure 5-2) in order to investigate the performance of the PSF-based iterative pattern refinement method and to determine the ultimate system performance. For the DMD-based high-precision beam shaper, the error can be generally categorized into experimental error and design error. Experimental error mainly contains camera measurement noise (speckle interference, photon noise, read-out noise, etc.) and system error (misalignment between the input Gaussian and the binary DMD pattern, optical component aberration, etc.). Design error is determined by the

blue-noise spectrum and pinhole LPF size. The PSF-based iterative pattern refinement corrects both types of error and the performance of this feedback process varies for different system bandwidths.

First, we compare the error level of a raw camera measurement before and after applying the digital LPF. The RMS error difference reflects experimental error for different system bandwidths. Since experimental error mainly contains high-frequency camera noise, it dominates the noise level of the raw measurement result at low system bandwidth. Therefore, the digital LPF filters out most of this error, revealing a high-precision beam profile. With the increase of system bandwidth, more design error in the blue-noise spectrum passes through the pinhole LPF. The low-pass-filtering effect of digital LPF therefore becomes less significant. The error level after the digital LPF approaches that of the raw measurement, and their error levels become comparable at high system bandwidth.

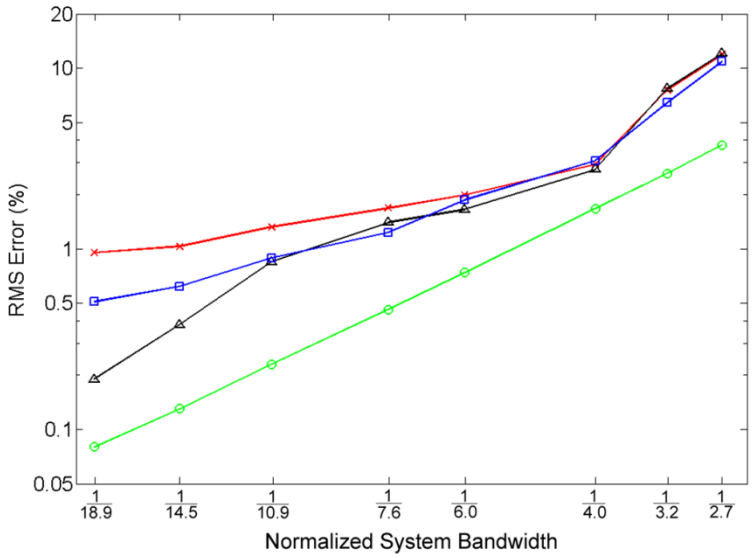

Figure 5-2: Intensity RMS error versus system bandwidth for the DMD-based high-precision beam shaper. Curves are for raw camera images (×), digital low-pass-filtered images (Δ), and simulated sinusoidal-flattop images (□) and also the computed digitization error (○).

Second, we investigate the performance of PSF-based iterative refinement by comparing the RMS error of low-pass filtered images to that of simulated patterns. Since the digital LPF has excluded most of experimental measurement error, the residue mainly includes remaining design error after the feedback process. The aim of PSF-based pattern refinement is to optimize the binary DMD pattern via a pixel-by-pixel adjustment. At low system bandwidth ($f < 1/14.5$), refinement accuracy is higher than the design error since the PSF peak amplitude is small. As a result, the low-pass-filtered result has a better image accuracy than the simulated pattern. Higher system bandwidth ($f > 1/14.5$) produces a PSF function with larger amplitude and therefore reduces refinement accuracy when adding or subtracting one PSF. Experimental results illustrate a comparable error level between PSF-based iterative pattern refinement and the error diffusion algorithm.

5.2 ARBITRARY BEAM PROFILE GENERATION TESTING

System evaluation based on the 2-D sinusoidal flattop beams enables us to predict image precision of any given target. In this section, we choose an actual image as the target for arbitrary beam profile generation [9] and use the beam shaping result to verify system evaluation.

5.2.1 Experimental conditions

A "Lena" image is superimposed on a flattop beam to form the Lena-flattop beam profile. The DMD in TI DMD Discovery 1100 developer's kit has a pixel size of $13.68 \times 13.68\ \mu m^2$. We use a 781 nm SMF-pigtailed laser diode (LPF-785-FC, Thorlabs) as the light source. This wavelength coincides with a diffraction efficiency peak for the

SLM. The two lenses in the telescope were chosen as 1000 mm and 750 mm focal lengths to give a -3/4 magnification.

Of the different spatial bandwidth images tested, two examples are selected to illustrate the system behavior: larger system bandwidth, f = 1/2.5, and smaller bandwidth, f = 1/6.7. To form the target image for each case, the original Lena-flattop beam profile was Gaussian low-pass filtered using two different bandwidths to confine its spatial spectrum: Gaussian filter half-width-half-maximum, HWHM = 1/3 and 1/11 respectively for the two cases. Numerical simulation showed that f = 1/2.5 and f = 1/6.7 were the optimized system bandwidths for these filtered target images. Consulting Fig. 5-2, one expects ~2% RMS error for the smaller bandwidth image based on the sinusoidal system performance evaluation. Similarly for the larger bandwidth image, the expected RMS error is ~11%. A simulated spectrum for the smaller bandwidth image as it is encoded onto the DMD is shown in Fig. 5-3. The image content is at the center, the blue noise due to the error diffusion encoding process is at high frequencies, and the location of the optimum system bandwidth (pinhole and digital low-pass filters) is indicated by the vertical lines. Note that although the optimum bandwidth is near the minimum of the spectrum, there is energy present at the sharp cutoff frequency.

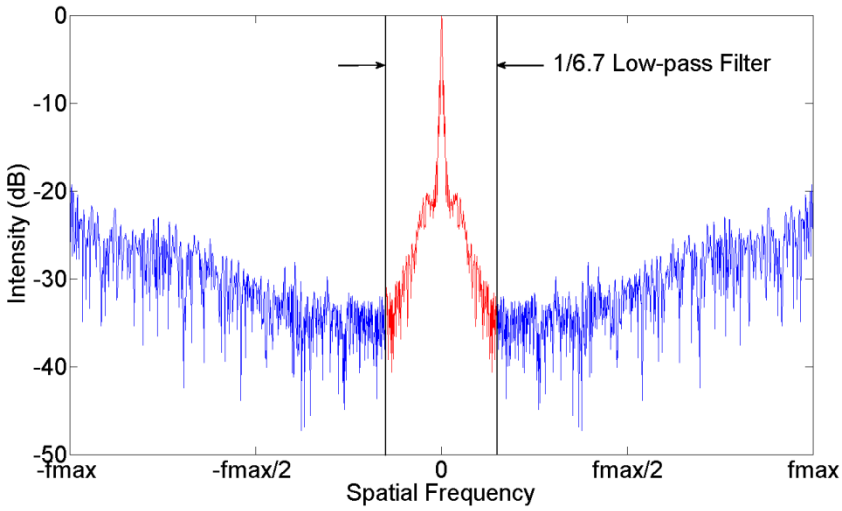

Figure 5-3: Cross section of the spatial frequency spectrum of the Gaussian low-pass filtered (HWHM = 1/11) Lena-flattop beam as encoded on the DMD showing rejected high frequencies (blue), accepted low frequencies (red), and the sharp-edged low-pass filter (vertical lines).

5.2.2 Experimental results

Experimental results for both filtered Lena-flattop beam profiles are shown in Fig. 5-4. The intensity RMS error is calculated by

$$RMS = \sqrt{\frac{1}{N} \times \frac{\sum_{(x,y)\in MA}\left(I_o(x,y) - I_t(x,y)\right)^2}{\sum_{(x,y)\in MA}\left(I_t(x,y)\right)^2}} \qquad (5\text{-}2)$$

where I_o and I_t are intensity profiles of the output beam profile and target image with equalized image power, and N is the total number of pixels within the measurement region, MA, which covers the entire "Lena" image area (3.08×3.08 mm^2). Compared to eq. (4-2), eq. (5-2) first calculates the standard deviation of raw intensity and then normalized this value with the average intensity in the measurement region. This

calculation approach avoids the singularity caused by the zero-intensity pixels in the output image.

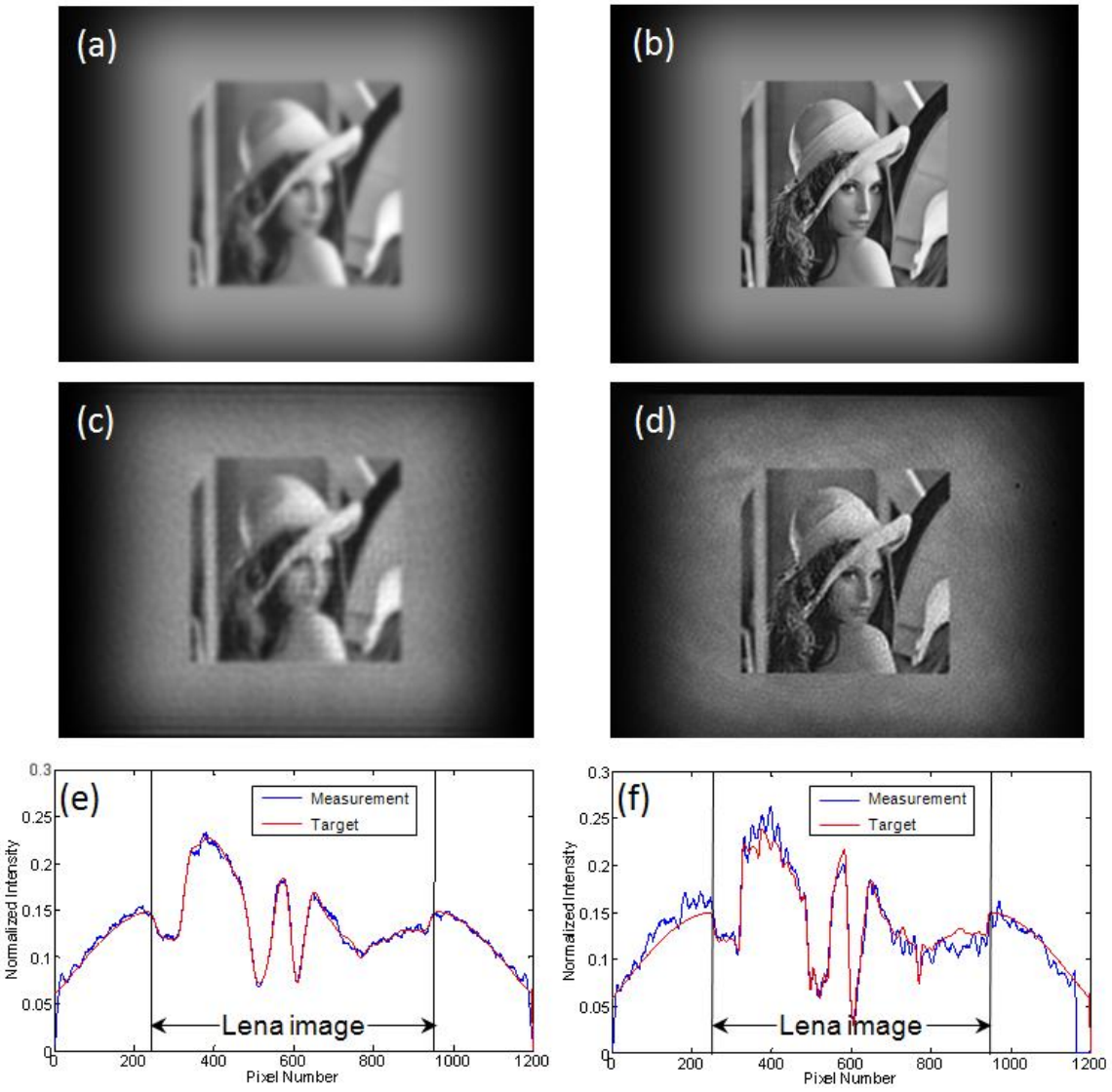

Figure 5-4: Lena-flattop beam profiles with f_N = 1/6.7 ((a),(c),(e)) and f_N = 1/2.5 ((b), (d), (f)) normalized system bandwidth. (a) and (b) are pre-filtered target images; (c) and (d) are output raw camera images; (e) and (f) are vertical cross sections through the raw output images and target images.

The output beam profile with smaller system bandwidth (f = 1/6.7) produced a raw RMS error of 3.11%. After the digital LPF, the RMS error was reduced to 1.97%. For the case of the larger system bandwidth (f = 1/2.5), more high frequency noise passed through the pinhole resulting in 10.02% RMS error for the raw camera image and 9.98% RMS error after the digital LPF. Values of RMS error for both cases have a good match with the expected values from the system performance evaluation using sinusoids.

The tradeoff between resolution and precision is clearly presented in these results; small system bandwidth reduces spatial resolution but increases precision (decreases error). As a result, a stronger image-blurring effect is observed in the output beam profile of Fig. 5-4(c). On the other hand, larger system bandwidth preserves the image sharpness and contrast as shown in Fig. 5-4(d). The major residual error in both output beam profiles comes from the ripple effect or orange peel effect observed in Figs. 5-4 (c-f). This ripple or ringing has been induced by the sharp-edged cutoff of the pinhole LPF. The ripples have a random orientation and their spatial frequency matches the spatial frequency of the system bandwidth. It is unavoidable unless an apodized pinhole was to be used.

5.2.3 Error analysis

We examined the statistical characteristics of the error in the output images. For example, error histograms for the Lena-flattop beam profile with f = 1/6.7 were calculated for both the raw image and the digitally low-pass filtered image. These histograms are shown in Fig. 5-5 and have been fit to zero-mean, normal distributions. The standard deviation, $\boldsymbol{\delta}$, is equal to the RMS error calculated from the corresponding image. Furthermore, the histograms conform closely to the normal fit and show little

asymmetry. We found this result indicative of a successful application of PSF-based iterative refinement while wider, skewed histograms indicated a malfunction in the system alignment or iterative refinement procedure.

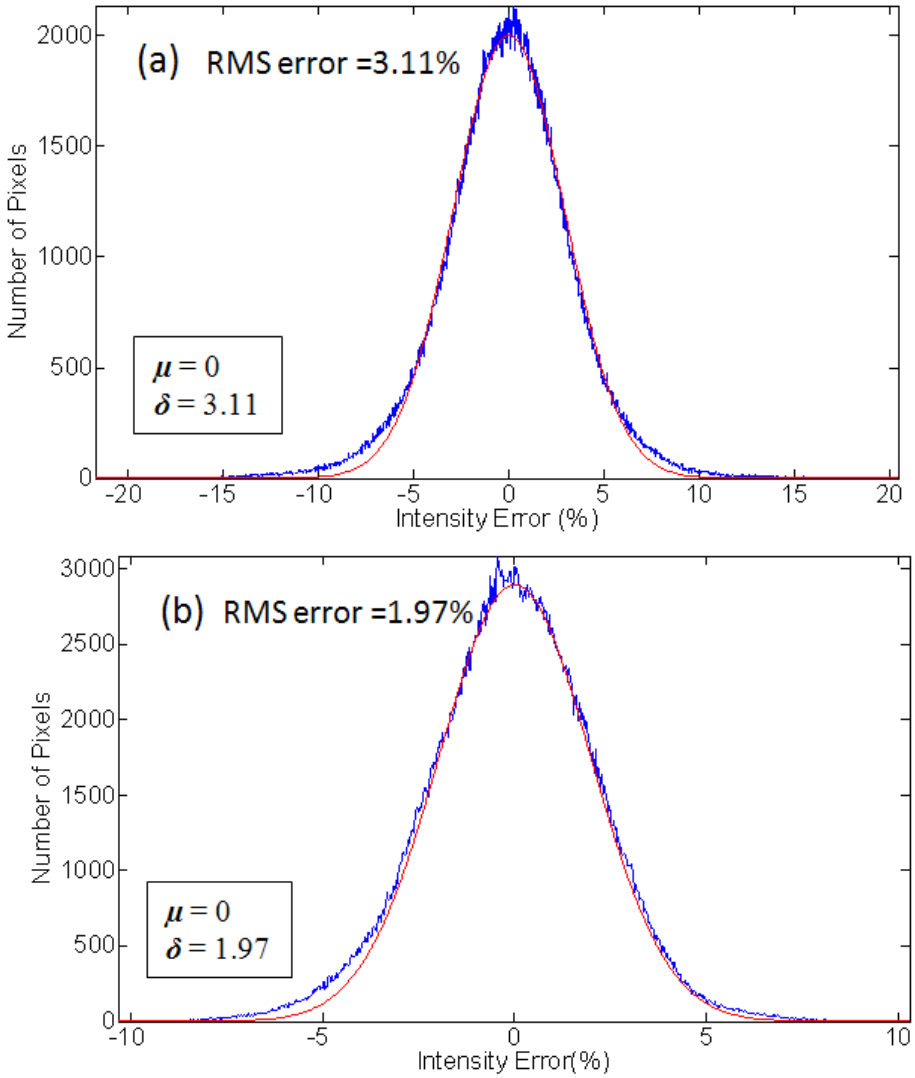

Figure 5-5: Histograms of residual error for the system bandwidth, f_N = 1/6.7, Lena-flattop beam profile (blue) from (a) the raw camera image and (b) after the digital LPF. Both curves are fit by Gaussian functions (red) (a) $y = 2001.3 \times \exp\left(-\frac{\varepsilon^2}{2\times 3.11^2}\right)$ and (b) $y = 2891.7 \times \exp\left(-\frac{\varepsilon^2}{2\times 1.97^2}\right)$.

5.3 SUMMARY

We have successfully demonstrated arbitrary laser beam profile generation by using the DMD-based beam shaper. The output error level versus system bandwidth for this system was evaluated by using sinusoidal-flattop beam profiles with different spatial periods. For arbitrary beam profile generation, example data were presented for Lena-flattop beam profiles with smaller and larger system bandwidths. The intensity RMS error of the measured profiles is consistent with the system evaluation result. We also demonstrated that the residual error mainly came from the ripple effect induced by the sharp-edged, low-pass filter and that this error followed a Gaussian distribution.

With the slowly-varying beam profile generation, we have completed the high-precision beam shape generation objective. The experimental results demonstrated that the DMD-based beam shaper is capable of generating various beam profiles with different spatial frequency spectra with low intensity RMS error. This system is ready to be implemented on an ultracold atom apparatus to dynamically control the spatial and temporal shape of the optical trap for the ultracold atoms in a Bose-Einstein condensate.

5.4 REFERENCES

[1] J. Liang, R. N. Kohn Jr., M. F. Becker and D. J. Heinzen, "Evaluation of DMD-based high-precision beam shaper using sinusoidal-flattop beam profile generation, " Proc. SPIE 8130, 81300C (2011).

[2] S. Zhang and P. S. Huang, "High-resolution, real-time three-dimensional shape measurement", Opt. Eng. 45, 123601(2006).

[3] D. Hong, H. Lee, M. Y. Kim, H. Cho and J. I. Moon, "Sensor fusion of phase measuring profilometry and stereo vision for three-dimensional inspection of electronic components assembled on printed circuit boards," Appl. Opt. 48, 4158-4169 (2009).

[4] M. G. L. Gustafsson, “Nonlinear structured-illumination microscopy: wide-field fluorescence imaging with theoretically unlimited resolution,” Proc. Natl. Acad. Sci. U.S.A. 102, 13081-13086 (2005).

[5] K. Genovese and C. Pappalettere, “Whole 3D shape reconstruction of vascular segments under pressure via fringe projection techniques,” Opt. Laser Eng. 44, 1311-1323 (2006).

[6] J. W. Goodman, “Introduction to Fourier Optics”, 3rd ed., Roberts & Company Publishers, Chapter 6 (2005).

[7] Sinusoidal MTF Optical Test Chart, Applied Image Inc., http://www.aig-imaging.com/Sinusoidal-MTF-Optical-Test-Chart.html, [Accessed at 8/1/2011].

[8] M. Fujiwara, M. Teshima, J. Kani, H. Suzuki, N. Takachio, and K. Iwatsuki, “Optical carrier supply module using flattened optical multicarrier generation based on sinusoidal amplitude and phase hybrid modulation,” J. Lightwave Technol. 21, 2705 -2714 (2003).

[9] J. Liang, S. Wu, R. N. Kohn, Jr., M. F. Becker and D. J. Heinzen, "Band-limited laser image projection using a DMD-based beam shaper", Proc. SPIE 8254, 825421 (2012).

Chapter 6 Homogeneous optical lattice generation using the DMD-based high-precision beam shaper

The previous beam shaping experiments have demonstrated high-precision flattop beams for various light sources that could be used to form either a standing-wave or thin optical lattice. In this chapter, we report the application of using beam shaping to generate a homogeneous one dimensional (1-D) standing-wave optical lattice of the correct dimensions for conducting cold atom experiments [1].

6.1 Experimental Setup

Figure 6-1 shows the optical layout of the homogenous 1-D optical lattice test bench configured to produce a standing-wave optical lattice of the correct size for cold atom experiments. The input quasi-Gaussian beam is expanded and collimated by a 5× telescope to best fit the DMD size. No spatial filtering is conducted for the input light. A pinhole, functioning as a spatial low-pass filter, is placed at the back focal plane of the first lens (f1). The pinhole diameter varies from 610 to 1200 μm, depending upon the input light source. The DMD, camera, and other optical elements are all perpendicular to the optical axis.

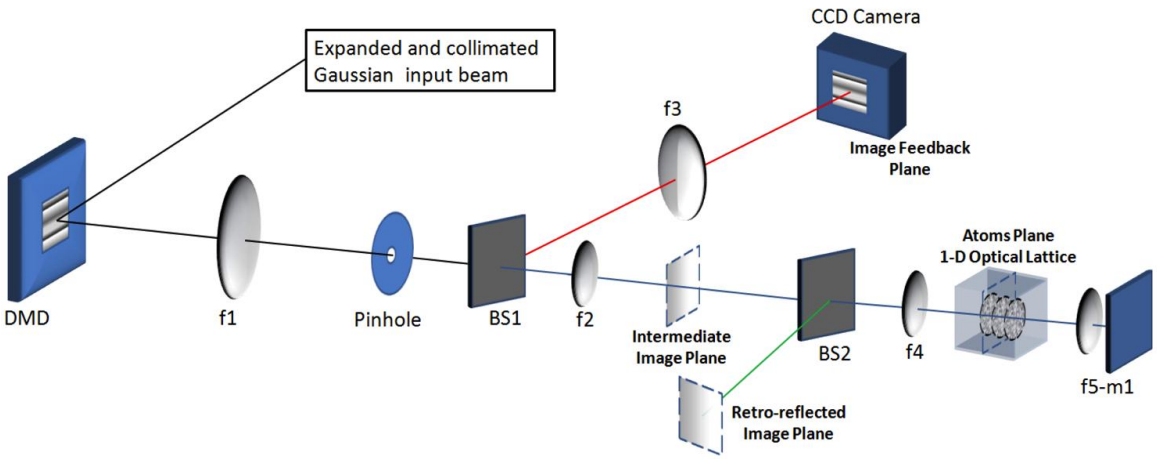

Figure 6-1: Optical layout of the homogenous 1-D optical lattice test bench. The first beam splitter (BS1) separates light into the image feedback arm (red) and the optical lattice arm. The second beam splitter (BS2) forms the retro-reflected image plane (green).

The light passing through the pinhole is split into the image feedback arm (f3) and optical lattice arm (f2). The image feedback arm is identical to the DMD-based beam shaper (Fig. 2-1) described in previous chapters. The telescope in the image feedback arm (f1 and f3) uses 300 and 250 mm or 500 and 400 mm focal length lenses to image the DMD with a magnification of -5/6 or -4/5. A windowless Spiricon CCD camera is placed at various diagnostic planes to monitor beam profiles. In the optical lattice arm, the beam size is reduced by the telescope (f1 and f2) and a following imaging lens (f4). The optical lattice beam is then retro-reflected by a lens-mirror combination (f5 – m1) to form the 1-D standing-wave optical lattice in a region smaller than 50 μm on a side.

6.2. HOMOGENOUS 1-D OPTICAL LATTICE GENERATION

Several system requirements need to be considered for optical lattice generation. First, we must calculate the required input laser power because the depth of potential wells relates to the light intensity. Second, the quality of the flattop beam is sensitive to

the camera gain non-uniformity and system alignment. Thus, an accurate system calibration is necessary to provide a uniform measurement base. Finally, the iterative refinement process was slow because it was operated off-line. Different software was used to control the camera, process the image, and load the DMD pattern. It was clear that integrated automation software should be used to increase the operation speed. Implementation of these objectives is described in the following sections.

6.2.1 System Preparation

We have chosen Rubidium-87 (^{87}Rb) atoms for our BEC experiment. A 1064 nm fiber laser is used to form the optical lattice. This wavelength is far away from the resonant frequency of Rubidium D1 ($5^2S_{1/2} \rightarrow 5^2P_{1/2}$) and D2 ($5^2S_{1/2} \rightarrow 5^2P_{3/2}$) transitions at 794 and 780 nm, respectively, but still maintains large enough optical dipole polarization to create a sufficient gradient force. In the BEC experiment, the dipole potential for standing wave needs to be much larger than the atom recoil energy, E_R, at the trapping laser wavelength in order to effectively confine atoms in the optical lattice. In our experiment, we would like to realize a dipole potential of $30E_R$, and this requires a laser intensity of I = 496 W/cm^2. For a 50×50 μm^2 flattop beam with the power conversion of 7%, the total power in the Gaussian beam is 1.26W for 1-D optical lattice generation.

6.2.2 System Calibration

System calibration is needed before running a beam shaping experiment. Specifically, users need to complete camera calibration tasks: white field measurement,

system alignment, scaling factor measurement (camera pixels to DMD pixels), and dark field subtraction.

First, white field measurement was conducted to correct for dust covered pixels and adjust the pixel gain. We placed an integrating sphere at the imaging plane of the image feedback arm. The output port was connected to the camera. In order to reduce the error introduced by photon noise and speckle interference, the low-pass filtered white field image was used to compensate the pixel gain non-uniformity. Then, we adjusted for dust-covered pixels by comparing the filtered image to the raw image, shown in Fig. 6-2. A selection algorithm was designed to compare the raw measurement to the low-pass filtered result for every pixel. If the difference was larger than the threshold (5% in the experiment), this pixel was considered as dust covered and the raw measurement intensity was replaced with the low-pass filtered image value.

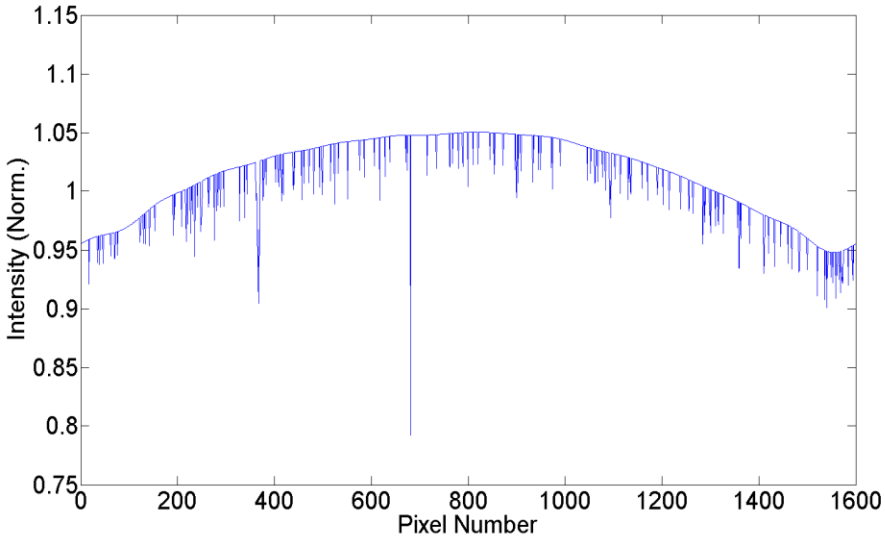

Figure 6-2: Cross section of the LPF image of the white field measurement showing camera dust.

Second, we carefully aligned the camera perpendicular to the incident beam. This process removed interference fringes caused by reflection and scattering light in the CCD sensor. Third, the size-scaling factor between camera pixels and DMD pixels was measured to convert the measurement profile at the image plane back to the DMD plane for pattern generation and refinement. Finally, pixel intensity error caused by the dark current in the CCD sensor was subtracted by the Ultracal! function [2] in the Spiricon laser beam profiler.

6.2.3 Lattice Beam Quality Measurement

The optical lattice beam needs to have a $50 \times 50\ \mu m^2$ flattop region to form a standing-wave optical lattice with ~100 lattice sites along each dimension. A two-stage imaging configuration is used in the optical lattice arm to reduce the size of the flattop beam from the DMD plane as shown in Fig. 6-1. For the first stage, a 100 mm focal length lens (f2) is paired with f1 to produce a -1/5 magnification telescope. This 5× reduced flattop beam is measured at the intermediate imaging plane. The beam is further reduced by another 100 mm focal length imaging lens (f4) to produce the optical lattice beam at the atoms plane. This lens is a doublet lens designed and AR coated for 780-1550 nm. Depending upon the beam size requirement, we adjusted f4 to achieve another 5 to 10 times reduction. Combined with the first stage, the size of the flattop beam is reduced by 25-50 times. In addition, we placed another beam splitter between f2 and f4 to create the third image plane that is equivalent to the intermediate imaging plane. This enables the measurement of the beam profile after retro-reflection and can be used to illustrate the beam quality of the optical lattice.

The LabVIEW-based system automation is used to control the beam shaping experiment. Beam profiles at various diagnostic planes were measured to examine the beam quality in the optical lattice arm. The raw RMS error for different measurement planes is summarized in Table 6-1. A flattop beam with RMS error of 1.15% was produced at the image feedback arm. In the optical lattice arm, measurement obtained 1.23% RMS error at the intermediate imaging plane. At the atoms plane, the intensity uniformity was maintained at 1.25% RMS error over the entire circular flattop region with a diameter of 70.4 μm (Fig. 6-3). After retro-reflection, the intensity uniformity was slightly degraded to 1.40%. The measurement result demonstrated a high uniformity of the flattop beam at the optical lattice arm. Our calculation shows that the focal depth (Rayleigh range) at the atoms plane is ~50 μm. For a 1064 nm laser beam, this enables us to make ~100 lattice sites in the longitudinal dimension and is more than sufficient for the ultra-cold atoms experiment. Furthermore, the Phase Transfer Function (phase part of the optical transfer function or OTF) for a well-behaved imaging system (near diffraction limited and focused) is flat [3]. Thus the phase in the various image planes, including the atoms plane, will correspond to the phase of the wavefront leaving the DMD. The phase wavefront measurement using a Michelson interferometer showed that the phase difference over the central part of the DMD (flattop region) is $<0.77\pi$ in the horizontal direction and $<0.16\ \pi$ in the vertical direction [4]. Outstanding DMD face flatness over the flattop region assures the production of an output beam profile with good phase flatness.

Table 6-1: Raw RMS error of measurement flattop beam in various diagnostic planes.

Measurement Plane	Image Feedback	Intermediate	Optical Lattice	Retro-reflected
Flattop Dia. (μm)	1760	352	70.4	352
Raw RMS Error (%)	1.15	1.23	1.25	1.40

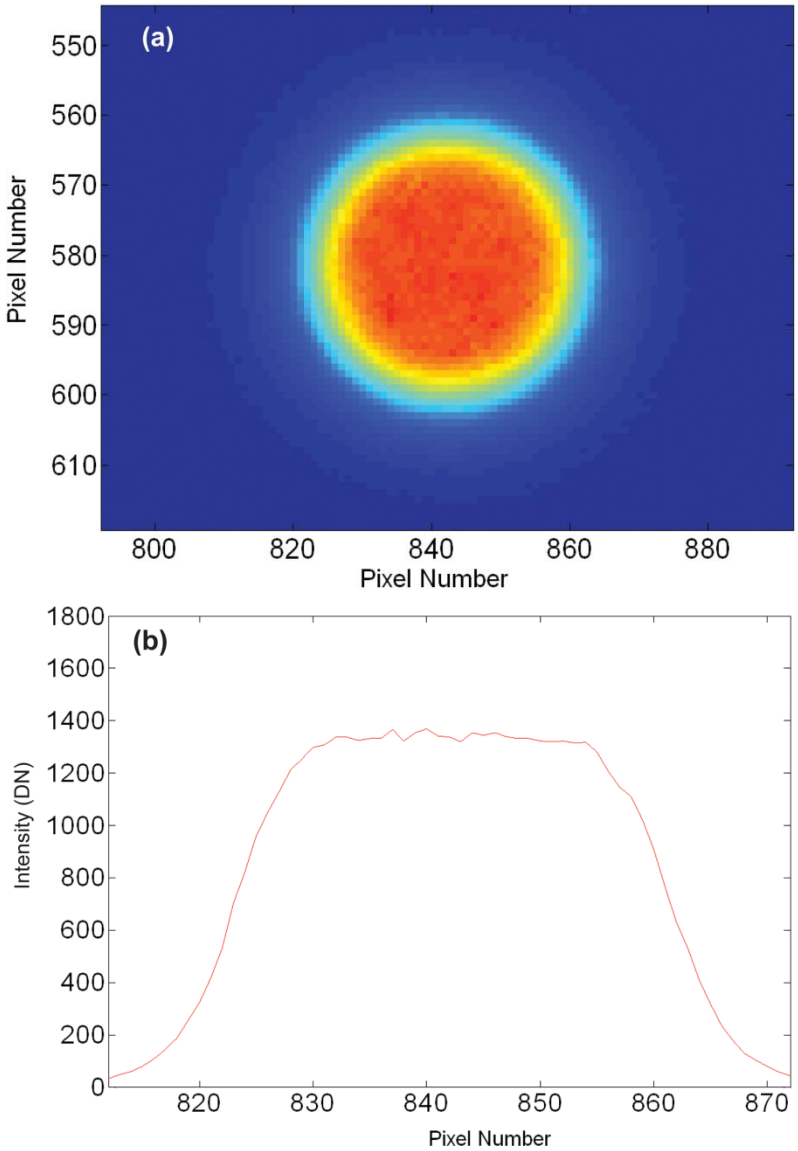

Figure 6-3: (a) Top view and (b) cross section of the flattop beam profile at atoms plane.

The entire beam shaping system is evaluated by comparing beam profiles at different diagnostic planes. We first discuss the beam profile quality at the intermediate image plane (see Fig. 6-1) that is reduced by a factor of 5 from the DMD and is not in the iterative refinement loop. The raw intensity uniformity at the intermediate imaging plane (1.23%) slightly increased compared to the beam profile measured at the image feedback arm (1.15%). After the digital LPF, the RMS error also increased from 0.2-0.3% (image feedback plane) to 0.7-0.9% (intermediate imaging plane). For the Spiricon camera with a certain sampling rate (4.4 μm pixel width), smaller beam dimension brings in the intensity-averaging effect, which should compensate a 4-time increase of the digital LPF size due to change of the telescope configuration (from f1-f3 to f1-f2) in these two arms. This indicates that the beam profile after iterative pattern refinement has some non-uniformity to the optical lattice arm. This non-uniformity could possibly come from the aberration between different lenses (f2 and f3), error residual in system calibration, and other measurement error from the camera.

Second, we examine the evolution of beam profile quality at the atoms plane. The raw RMS error is essentially unchanged from the intermediate imaging plane to the optical lattice plane. Intensity uniformity after the digital low-pass filter is comparable as well. This result demonstrates that the single imaging lens (f4) does not further degrade the beam profile. In addition, the impact on the beam profile of the entire optical lattice arm is analyzed by comparing measurement results at the retro-reflected image plane to the intermediate imaging plane. The raw RMS error of the flattop beam increased by 0.17% after a round trip through the focusing and retro-reflection optics surrounding the atoms plane. This small degradation is mainly caused by various optical elements in the optical lattice arm. Thus, we have demonstrated that the optical lattice arm has little impact on the beam quality. The experiment verifies that this system was capable of

producing a high-quality flattop beam profile through the optical lattice volume both for the incident and retro-reflected beams.

The system evaluation concludes that the main error residue of the flattop beam at the optical lattice arm is still from the intensity non-uniformity of the beam profile, and it is caused by the non-equivalent performance of beam shaping between the image feedback arm and the optical lattice arm. For the future, we propose to conduct further pattern refinement based on measurements of the cold atom distribution, which is even more sensitive to small variations in the optical field. This approach should remove most RMS residue and improve intensity uniformity of the optical lattice beam.

6.3 SUMMARY

We demonstrated that precise flattop laser beams could be generated and retro-reflected while maintaining its flattop quality. The energy requirement for a 1-D standing-wave optical lattice was calculated for a 1064 nm laser beam. In addition, various system calibrations were conducted to improve the measurement accuracy. The size of the flattop beam was reduced by a factor of 25-50 by the telescope followed by an imaging lens. At the atoms plane, we produced a 1.25% RMS error circular flattop beam with diameter of 70.4 μm. This beam was retro-reflected to form the optical lattice at the atoms plane. The measurement of the retro-reflected beam profile illustrated a good intensity uniformity at the optical lattice. These results indicate that the generated homogenous 1-D optical lattice is sufficient for use in a quantum emulator using ultracold atoms.

6.4 REFERENCES

[1] J. Liang, R. N. Kohn, Jr., M. F. Becker, and D. J. Heinzen, “Homogenous 1-D optical lattice generation using a Digital Micromirror Device-based high-precision beam shaper”, J. Micro/Nanolith. MEMS MOEMS 11(2), (2012)

[2] Ophir-Spiricon, LLC, “LBA-FW-SCOR User Manual,” pp. 98 – 99 http://www.ophiropt.com/laser/register_files/lbafwscor.pdf, accessed [2/14/2012].

[3] J. Goodman, “Introduction to Fourier Optics”, 3rd. edition, Chapter 6 pp. 135-145, Roberts and Company Publishers, 2004.

[4] J. Liang, R. N. Kohn Jr., M. F. Becker, and D. J. Heinzen, "High-precision laser beam shaping using a binary-amplitude spatial light modulator," Appl. Opt. 49(8), 1323-1330 (2010).

Chapter 7 High-precision laser beam shaping for dynamic optical trap generation

In this chapter, we present another application using the DMD-based high-precision beam shaper to form dynamic optical traps. After a short review of previous approaches for optical trap generation, we describe the method of programming the DMD to generate useful patterns of traps. Experimental results of various mimicked Laguerre-Gaussian and Hermite-Gaussian profiles are presented. We also discuss the system performance by comparing the proposed method with the holographic optical tweezers.

7.1 INTRODUCTION TO OPTICAL TWEEZERS

Optical tweezers, first introduced by Ashkin et al. [1,2], have been used widely in many applications, such as biology [3,4], cold atom physics [5], material engineering [6]. Numerous groups have used various methods to engineer optical tweezers [7-10]. However, most of these passive approaches cannot achieve addressable control of the number of traps, their size or position; and these disadvantages stimulated the development of dynamic optical trapping via advanced trap geometries [11-13]. For instance, multiple optical trap sizes were generated via a micro-lens array [11]. Addressable control of these optical traps can be realized by using either a VCSEL array [12] or scanning a single laser beam over different locations with the help of an acoustic-optic modulator [13].

However, the most popular approach to create reconfigurable patterns of traps involves the use of spatial light modulators (SLMs). Because of their unique ability for amplitude and/or phase modulation, a spatial light modulator enables shaping the input beam into a nearly limitless number of possible beam profiles. The successful

implementation of the spatial light modulator in optical trapping has led to the use of holographic optical tweezers (HOE), in which a liquid-crystal phase-only SLM was used to create a spot array to trap the micro-particles in three-dimensions [14,15].

In addition, Laguerre-Gaussian (LG) or Hermite-Gaussian (TEM) light beams can be created by encoding proper phase gratings onto a liquid crystal SLM. As the solutions of Helmholtz equation in radial or Cartesian coordinates, these two series of beam profiles produces multiple optical traps simultaneously. Moreover, the helical phase front of the LG beam can be used for rotating trapped particles by interfering with a plane wave [16] or its mirror image [17]. However, the low energy damage threshold and relatively slow refreshing rate of the liquid crystal SLM excluded it from operating with high-energy laser sources and fast dynamic optical trapping.

The emergence of the Digital Micromirror Device (DMD) has enabled major advances in numerous areas in science and engineering [18]. Recent development of the DMD-based optical tweezers provided an alternative approach to generate addressable optical traps [19,20]. The DMD has a faster operation speed and does not need refresh or polarity reversal compared to the liquid crystal SLM. In addition, because binary amplitude modulation is realized through bi-state latching of an individual pixel, it has a full modulation depth in a broad wavelength range. Finally, it has a comparatively high laser damage threshold [21]. All these advantages make the DMD a good candidate for generating dynamic optical traps.

Ren et al. [22] utilized the DMD for LG mode generation. However, the binary-amplitude modulation produced low-quality reconstructed images as expected. Although dithering the mirrors helped create grayscale images, it is only suitable for white light (i.e. broadband) illumination [23] but not for coherent light sources. Second, the energy losses in the binary-amplitude hologram and in the zero order diffracted beam

significantly reduced the energy efficiency and useful bandwidth. Essentially, the lack of phase modulation limited the use of DMD for dynamic HOE generation. A recent design for dynamic control is realized by turning on or off either a single micromirror [21] or a patch of DMD mirrors [19], which cannot produce an arbitrary pattern of traps.

We propose a novel design of dynamic optical trap generation by a DMD-based optical system. This approach overcomes these limitations from the previous designs. It is capable of generating arbitrary patterns of optical traps with high image precision. Other advantages include broadband wavelength operation range, fast operation speed, and high power tolerant optics. In the first step to complete these goals, we demonstrate the capability of high-precision pattern generation and dynamic performance of this system by using sophisticated control of the DMD. This first step is the subject of this chapter. For the future, we plan to dynamically trap actual micro-particles or biological samples to test the system.

7.2 METHOD

7.2.1 Schematic configuration

The schematic configuration for DMD-based dynamic optical trap generator is shown in Fig. 7-1. The input quasi-Gaussian beam is expanded and collimated by a 5× beam expander to best fit the DMD. No spatial filtering is conducted for the input light. The incident beam propagates through a Fourier lens (f1) and an adjustable pinhole is placed at the back focal plane of this lens. The pinhole serves as a low-pass filter (LPF) and varies from 5.5 to 15.6 mm depending on the input laser wavelength.

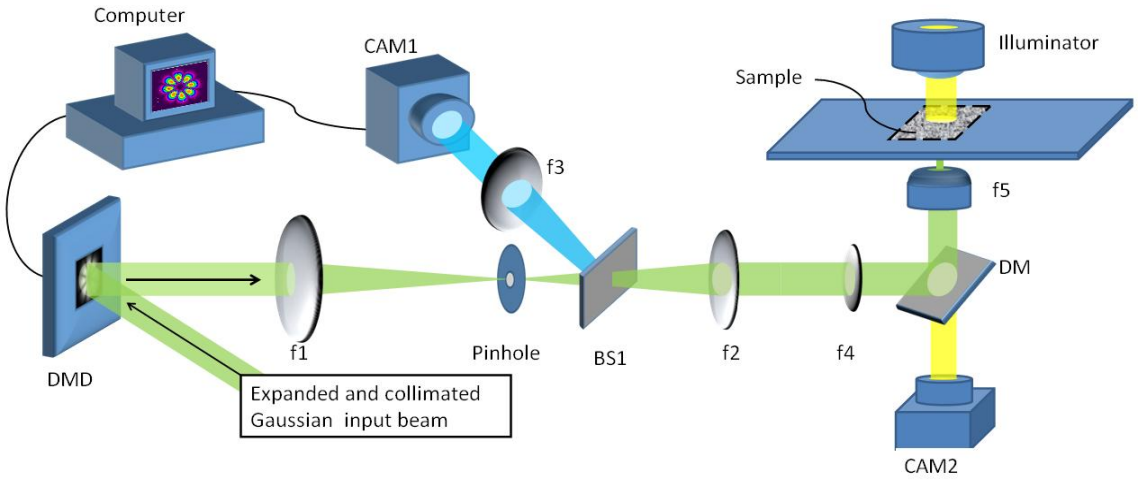

Figure 7-1: Schematic configuration for DMD-based optical trap generator.

The light passing through the pinhole is split into the image feedback arm (f3) and optical tweezers arm (f2). The image feedback arm is identical to the DMD-based high-precision beam shaper described in the previous chapters. Both f1-f3 and f1-f2 form two 4f telescope systems to image the binary DMD pattern to output planes with different magnification ratios. A windowless Spiricon CCD camera (CAM1) is placed at image feedback plane to monitor and diagnose beam profiles. In the optical tweezers arm, after the first relay optics stage (f1-f2), the shaped beam propagates through f4 and is transferred into the entrance pupil of a high numerical-aperture (NA) objective (f5) in an inverted optical microscope. A dichroic mirror (DM) reflects the laser beam while passing images trapped particles to a camera (CAM2). Lenses f4 and f5 form the second 4f telescope system to further reduce the beam size to form desired patterns of optical traps.

7.2.2 Programming the DMD to make patterns of optical traps

Unlike a holographic system, the desired pattern of optical traps is formed by imaging the amplitude profile encoded on the DMD to the sample plane. The following summarizes the beam shaping procedures that are given in detail in Chapter 3[24, 25]. The spatial reflectance of the DMD is calculated by the ratio of the desired pattern to the input quasi-Gaussian beam that has been accurately measured by the camera in the image feedback arm. This continuous reflectance function is converted by the error diffusion algorithm [26] to the initial binary pattern to be loaded onto the DMD. The spectrum of this binary pattern is spatially confined by the pinhole LPF by filtering out all high spatial frequency introduced by the binary amplitude modulation. Thus, band-limited image projection [27] transfers the binary DMD pattern back to a grayscale image.

The binary DMD pattern is refined iteratively based on the amplitude error image calculated from the error between the desired pattern and repeated measurements of output beam profiles. This refinement process is based on the point spread function (PSF) that represented the system bandwidth, and it determines the theoretical limit of the image precision and spatial resolution [28].

7.3 EXPERIMENTAL RESULTS

7.3.1 Experimental conditions

Because the main subject of this chapter is to demonstrate the high-precision performance of the DMD-based beam shaper for dynamic optical trap generation, we shall focus on the high-precision beam shaping in the image feedback arm (f1-f3) and the first stage (f1-f2) of the optical tweezers arm. In the experiment, we used a TI DMD Discovery 4000 developer's kit with the DMD chip that has a pixel size of 13.68×13.68

μm^2 to shape the beam from a 1064 nm fiber laser to form the desired pattern of optical traps.

Various high-order beams, such as Laguerre-Gaussian (LG_{pl}), Hermite-Gaussian (TEM_{nm}), Ince-Gaussian (IG) and Bessel patterns are desirable for creating complex optical traps. For our design, we selected amplitude profiles of LG_{pl} and TEM_{nm} beams to demonstrate the DMD-based beam shaper for optical trap generation. It is important to point out that due to the amplitude-only modulation of the DMD, intensity profiles of the LG_{pl} and TEM_{nm} beams are used as the target function. Thus, the generated beam profiles are not exact solutions to the Helmholtz equation but only have the desired intensity (denoted as $|LG_{pl}|^2$ and $|TEM_{nm}|^2$) with a nearly flat phase front so that they only mimic LG_{pl} and TEM_{nm} beams.

7.3.2 Beam shaping in the image feedback plane

In the image feedback arm, the two lenses in the telescope were chosen as 1000 mm and 750 mm focal lengths to give a -3/4 magnification. The measured beam profiles of various orders of $|LG_{pl}|^2$ and $|TEM_{nm}|^2$ beams are illustrated in Fig. 7-2. The experiment demonstrated that the input quasi-Gaussian beam was transformed into the desired beam shapes.

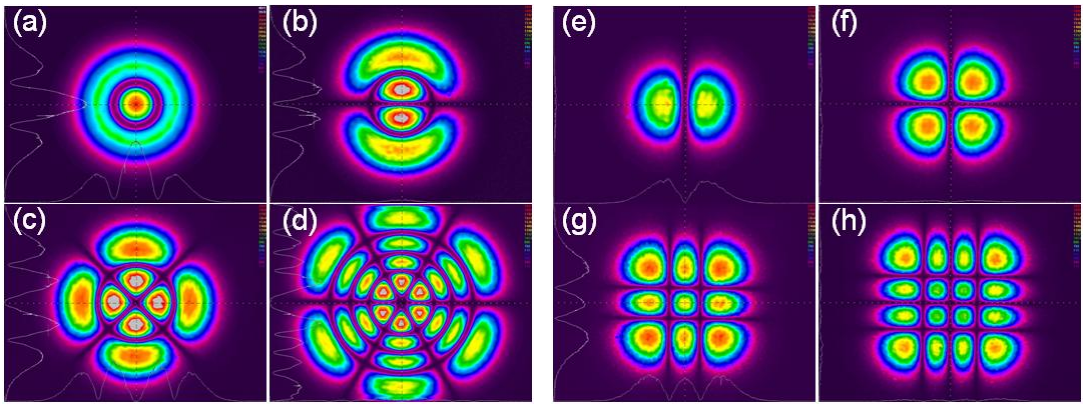

Figure 7-2: Measured beam profiles in the image feedback arm. (a) $|LG_{01}|^2$, (b) $|LG_{11}|^2$, (c)$|LG_{22}|^2$, (d)$|LG_{33}|^2$ and (e)$|TEM_{01}|^2$, (f)$|TEM_{11}|^2$, (g)$|TEM_{22}|^2$, (h)$|TEM_{33}|^2$.

In order to quantitatively analyze the image precision of these beam profiles. The averaged root-mean-square (RMS) error was calculated by

$$RMS = \frac{1}{I_m} \times \sqrt{\sum_{(x,y)\in MA} [I_o(x,y) - I_t(x,y)]^2} \tag{7-1}$$

where $I_o(x,y)$ and $I_t(x,y)$ are intensity profiles of the output beam and the desired pattern. These two intensity profiles are adjusted to have the same total energy before the RMS error calculation. The measurement region (MA) is a 500×500 square (2.2×2.2 mm^2) to cover the entire beam profile region. The summation within the square root calculates the standard deviation of the raw measurement image, and it avoids the singularity when dividing by zero-intensity points in the image. This standard deviation of the output beam profile is normalized by the intensity mean, I_m, within the measurement region.

The RMS error of generated beam profiles (Table 7-1) illustrated a clear tradeoff between the image precision and spatial resolution. As the pattern became more

sophisticated, higher spatial resolution required larger system bandwidth that reduced the image precision. As a result, the RMS error increased from approximately 3.8% ($|TEM_{01}|^2$, $|LG_{01}|^2$) to around 4.7% ($|TEM_{33}|^2$, $|LG_{33}|^2$).

Table 7-1: The normalized bandwidth and RMS error of generated LG and TEM beam profiles.

Beam profile	$\|TEM_{01}\|^2$	$\|TEM_{11}\|^2$	$\|TEM_{22}\|^2$	$\|TEM_{33}\|^2$	$\|LG_{01}\|^2$	$\|LG_{11}\|^2$	$\|LG_{22}\|^2$	$\|LG_{33}\|^2$
Bandwidth[1]	0.14	0.15	0.18	0.18	0.15	0.18	0.18	0.20
RMS error (%)	3.88%	4.22%	4.66%	4.77%	3.84%	4.30%	4.39%	4.71%

[1]The bandwidth is normalized by the maximum system bandwidth of (2x DMD pixel pitch)$^{-1}$. $fm = 36.55$ mm^{-1}

High-speed dynamic control is another major feature of the DMD-based approach to generate the pattern of optical traps. Supplementary Media 7-1 (Fig. 7-3) shows the beam profile first rotated counter-clock wise, shrunk and expanded in size, and rotated back clockwise. This process is completed by loading over 80 pre-calculated binary DMD patterns. For our Discovery 4000 with a USB 2.0 port, we achieved an operation speed of 34.6 frames/second.

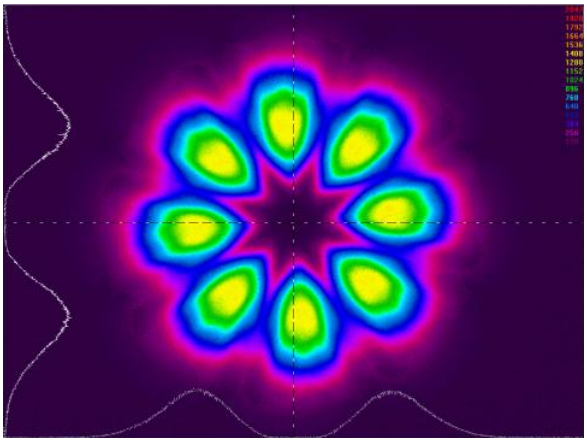

Figure 7-3: The dynamic control of a moving $|LG_{04}|^2$ beam profile. A 70ms delay is added between each frame to accommodate the low speed video capture software. (Media 7-1)

7.3.3 First stage of the optical tweezers arm

In the optical tweezers arm, the 100 mm focal length lens (f2) demagnifies the binary DMD pattern by 10 times. The shaped beam profiles are measured at the 1/10x reduction image plane. In the following section, we choose the amplitude profile of TEM_{01}* mode (the "donut" mode) as an example of a dark optical trap to analyze the characteristics of the output beam profile and approaches to improve its quality.

For the first-generation donut beam, the raw measurement (Fig. 7-4(a)) achieved a relative large RMS error at the 1/10x reduction image plane. The iterative PSF-based feedback only slightly improved the image quality.

In the ideal "donut" mode, the intensity profile goes down to zero at the center and quickly bounces back, forming a sharp "V" at the center (Fig. 7-4(b)). This feature carries high spatial frequencies that are filtered out by the pinhole low-pass filter. Therefore, the maximum in the amplitude error image is located at the image center. In the PSF-based iterative pattern refinement, the refinement starts at the center (maximum error). However, we found that turning off any DMD pixel increases the RMS error in the

error image. Thus, the refinement will stop almost immediately. Although the quality of the output beam profile can be improved by adjusting DMD pixels in the surrounding area (blocking out the central part of the error image), the maximum error at the center hindered significant image enhancement.

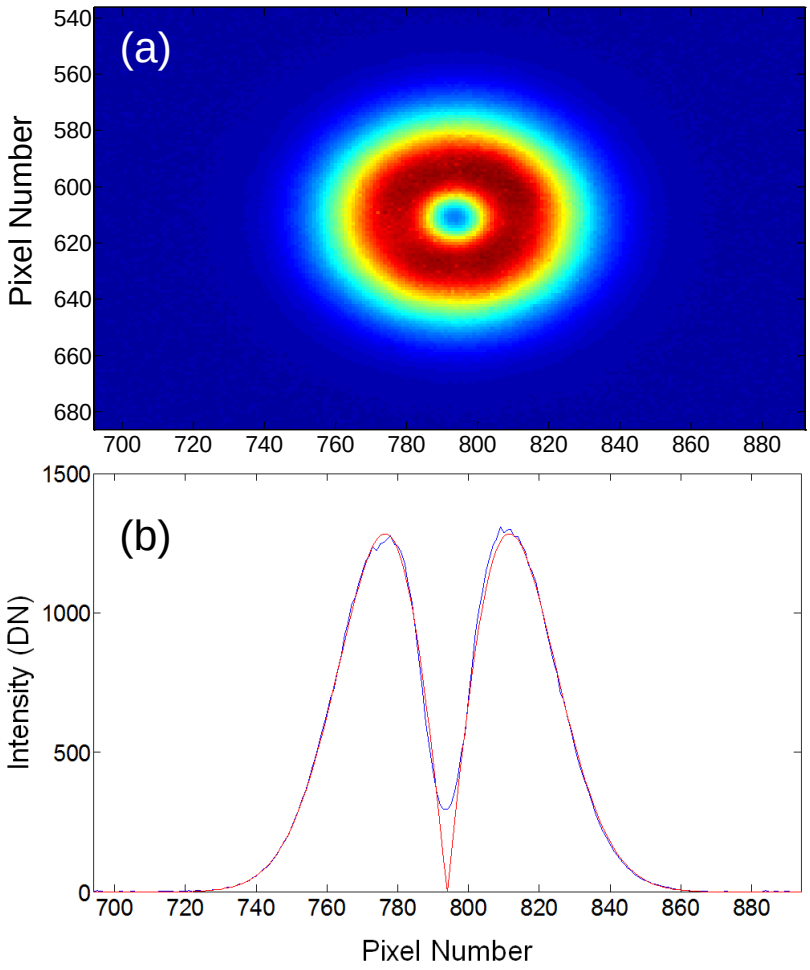

Figure 7-4: Dark trap generation at the 1/10x reduction image plane using a mimicked donut mode. (a) Top view and (b) horizontal cross section of the raw measurement beam profile. The experimental result (blue) is compared with the target function (red).

The band-limited projection of the DMD-base beam shaper reduced the contrast of the dark trap. This effect could also exist in other optical trap generation approaches as

long as the system cannot preserve all required spatial frequencies. In order to overcome this intrinsic shortcoming of the donut mode, we propose to use a cosine-tapered ring shape to mimic the "donut" shape. The cosine-taped ring should be able to create an adjustable, flat dark region at the center, which confines the major spatial spectrum to low frequencies. As a result, the sharp tip in the "donut" shape is replaced by a flat zero-intensity region connected by two cosine functions (Fig. 7-5). More importantly, simulation showed that the beam profile of the cosine-tapered ring is well preserved after a small pinhole low-pass filter (system bandwidth of $f = 0.07$).

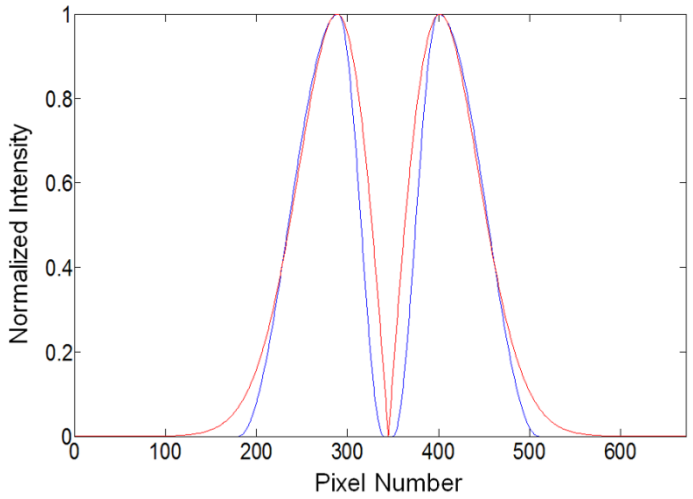

Figure 7-5: Amplitude profiles of a donut laser mode (red) and the cosine-tapered ring shape (blue).

This cosine-tapered ring shape was implemented in the beam shaping experiment. The PSF-based iterative pattern refinement was conducted for 5 times to reach the minimum RMS error at the image feedback plane. The experiment produced a good quality cosine-taped ring profile with a good match of the target function at 1/10x reduction plane (Fig. 7-6). The RMS error over the entire beam profile for a raw

measurement image was 2.31% (Diameter = 60 pixels). The central part of the beam profile had a deeper trap depth compared to in the "donut" mode generation experiment. These results showed that the cosine-taped ring shape improved the trapping depth with larger image contrast. In addition, we can control the width, depth, and shape the of the trap, enabling more flexible control of the trap for manipulating small particles.

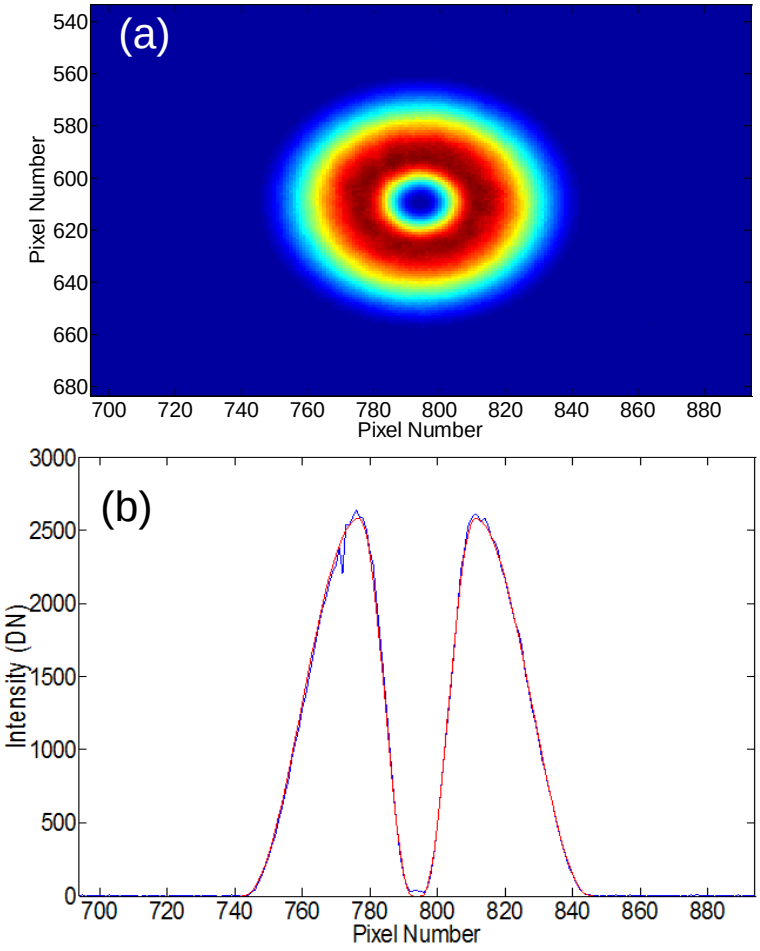

Figure 7-6: Dark trap generation at the 1/10x reduction image plane using the cosine-taped ring profile. (a) Top view and (b) cross section of the raw measurement beam profile. The experimental result (blue) is compared with the target function (red).

The evolution of the dark trap in the beam propagation direction (through focus) was examined to study the working distance of the optical traps in this dimension. Defined as the tolerance of the placement of the image plane, the depth of focus (DOF) is used to determine maximum length for the patterns to retain their shape. The DOF is calculated by

$$\Delta f_1 = 2.44(F/D)^2 \lambda \qquad (7\text{-}2)$$

where λ is the laser wavelength, F is the focal length, and D is the entering light diameter instead of the lens aperture. For the 1/10x image plane, D = 5.45 mm for the normalized system bandwidth of f = 0.07, because the bandwidth of the DMD-based beam shaper is controlled by the pinhole size and not by the finite aperture of the imaging lens. Assuming that the small increase in beam diameter between the pinhole and lens f2 can be ignored, then D is equal to the pinhole diameter. The DOF of the dark trap is calculated to be $\Delta f1 = 0.87$ mm.

The experiment was conducted at the 1/10x reduction plane for the dark trap profile by measurement of beam profiles through focus (Fig. 7-7). The pattern maintained its ring shape in the range ±1 mm while degrading quickly to an asymmetric profile with the central hole filling in as it propagated away from the image plane.

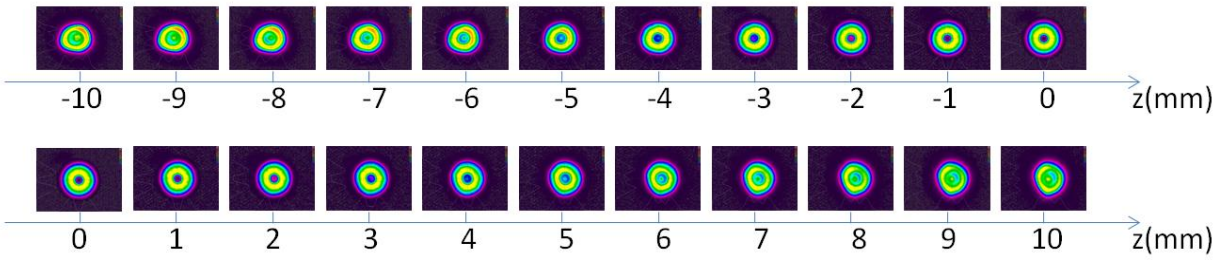

Figure 7-7: Top view of the raw camera images of the dark trap (cosine-taped ring shape) in different measurement planes along the z-axis.

A more detailed analysis was conducted by examining the cross section of these beam profiles (Fig. 7-8). The central intensity quickly increased from 0 at the 1/10x reduction image plane to around 1700 digital numbers (DN) at z = ±5 mm, which significantly reduced the trap depth. This suggests that the alignment will be sensitive in the z direction between first image reduction stage and the following microscope.

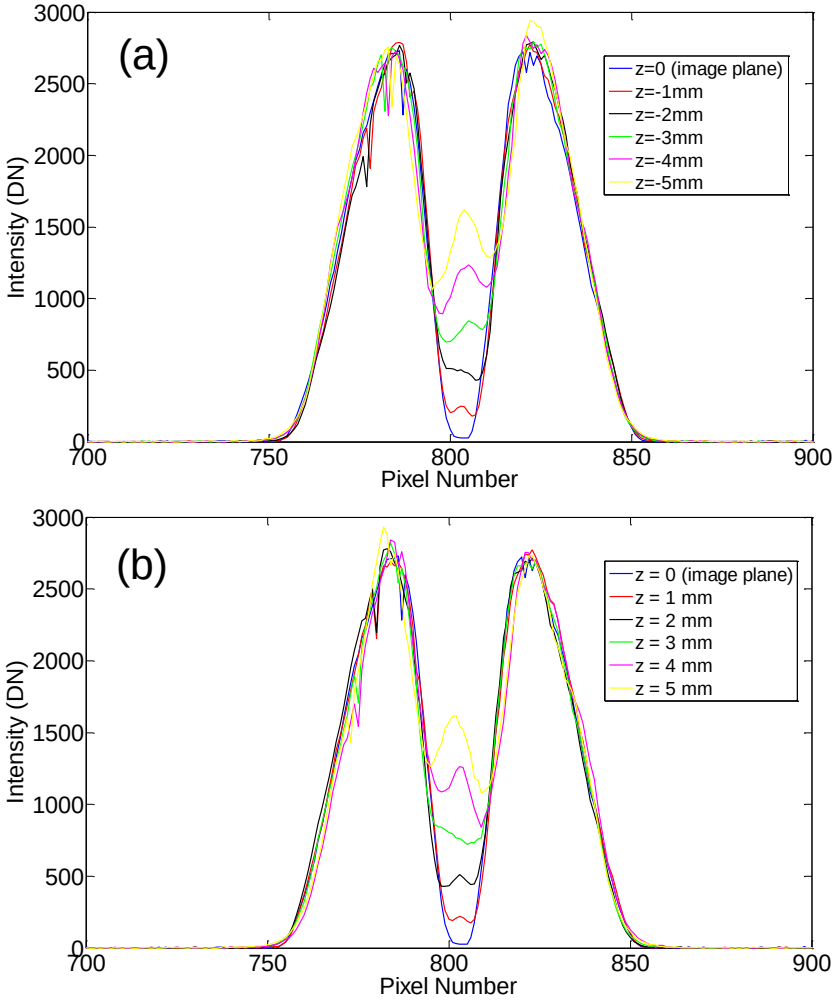

Figure 7-8: Horizontal Cross sections of the cosine-taped ring profile at different measurement planes of (a) z = -5 to 0 mm and (b) z = 0 to 5 mm.

At the 1/100x image plane (sample plane), the DOF of the second stage controls the trapping depth and depends upon the specific objective lens in the microscope. As an example, we use a standard 10× IR objective lens (LMH-10x-1064, effective focal length f_e = 20 mm, Thorlabs) to calculate the DOF. The laser beam enters the objective lens with the approximate size of D = 1.8 mm based on measurement in the system. The calculated DOF is $\Delta f2$ =0.32 mm at 1/100x plane.

For other magnification ratios, the calculated DOF is 1.28 mm for a 1/50x system (LMH-5x-1064, f_e = 40 mm, Thorlabs) and 0.08 mm for a 1/200x system (LMH-20x-1064, f_e = 10 mm, Thorlabs). In summary, the DMD-based system shows a reasonable depth of focus tolerance based on the DOF calculation at the 1/10x image plane and on measurements of the beam profile through focus. At the sample plane, low f-number objective lenses would constrain the trapping operation to a 2-D (x-y) plane due to small DOF. On the other hand, examples were given with higher f-number systems that show DOF in the mm range at the sample plane.

7.4. DISCUSSION AND COMPARISON

In this section, we further discuss performance of the DMD-based optical trap generator and compare it to the HOE. Both approaches are capable of generating various patterns of optical traps with a dynamic control. The ability of arbitrary beam profile generation is particularly good for traps with elongated or other irregular shapes [29]. On the other hand, the DMD-based system is distinct from the HOE in aspects of energy efficiency, control flexibility, and pattern generation.

7.4.1 Energy efficiency

Faustov et al. [21] tested the DMD damage threshold by focusing the entire power of a laser in visible (633 nm) and infrared (1064 nm) wavelengths to a single micromirror (13.68 x 13.68 um^2). No damage was observed for input powers below 30 mW. In addition, the global damage threshold of the DMD chip is measured to be 20W/cm^2 for visible wavelengths and 10W/cm^2 in the infrared [30]. On the other hand, the reported average power damage threshold of a commercially available liquid crystal SLM is 1-2 W/cm^2 [31].

The energy diffraction efficiency of the DMD can be calculated by eqs. (4-6) in Chapter 4, and we reiterate here that the diffraction efficiencies of several typical wavelengths are 72.78% (633 nm), 52.98% (1064 nm), while the 750-800 mm window satisfies the blaze condition to obtain near 100% diffraction efficiency. Another major energy loss comes from the DMD binary pattern, and the typical Gaussian-to-output beam profile conversion efficiency is 40-60%. Considering other energy loss from the micromirror reflectivity, area fill factor, and the window reflection, the overall energy efficiency for the DMD-based beam shaper is around 10-20%. On the other hand, the diffraction efficiency of the liquid crystal SLM is generally independent of the operation wavelength and depends mainly on the area fill factor. Therefore, the liquid crystal SLM is able to achieve a 40-60% overall energy efficiency.

7.4.2 Control flexibility

The fast operation speed is a major advantage of DMD-based optical trapping. Although the performance reported in this chapter is 34.6 Hz, it is possible to achieve a frame rate up to 26.6 kHz [32] by using the fast I/O connector. In addition, the phase modulation from a liquid-crystal SLM requires the input light to have good coherence

and polarization purity. The operation wavelength is also specified for the corresponding SLM in order to achieve a full 2π phase modulation. These requirements limit the available light sources and potentially increase the complexity of the optical system. On the other hand, DMD has the same binary modulation for all input wavelengths, meaning it can be operated with a wide range of coherent and incoherent light sources at different wavelengths [33]. Thus, the same DMD device with a broadband AR coated cover window is suitable for generating optical trapping using several different laser wavelengths.

7.4.3 Pattern generation

In terms of pattern generation, the DMD has unique advantages in the intensity precision of the generated beam profiles. As demonstrated in Section 7.3.3, the DMD-based beam shaper produced an improved dark trap pattern, and can produce any designated beam profile with a predictable error level. Considering the major frequency content of a typical optical trap or target image is within 1/3 of the normalized system bandwidth, the DMD-based beam shaper is capable of generating nearly any complex profile with < 10% RMS error. On the other hand, holographic reconstructed images from a phase-only liquid crystal SLM only produce the approximation of the desired pattern because the magnitude is not modulated. Other byproducts, such as twin images and the zeroth-order diffracted beam, also reduce the image quality of holographic optical tweezers.

However, the lack of phase modulation ability restricts that the generated beam profiles from the DMD-based beam shaper. They will have a wave front that matches the surface curvature of the DMD. This restriction does not exist for the liquid crystal SLM

so that it is possible to encode advanced phase patterns to produce optical vortices for 3-D trapping as well as compensate for SLM surface curvature. In addition, the HOE approach can produce beams with phase and amplitude matching wave equation solutions and so these beams are self-replicating as they propagate. Although the beam size will change through focus, the pattern will be unchanged except for size scaling. However, the DMD-based optical trap can only manipulate the trapped particles in the depth of focus region.

7.5 SUMMARY

In this chapter, we presented a novel approach for creating dynamic optical traps by using a DMD-based beam shaper. The amplitude profiles were encoded as binary DMD patterns and converted to the desired patterns by a 4f imaging system with a pinhole low-pass filter. A 1:10 telescope reduces the beam size for the first stage of the optical tweezers arm. The demagnified beam profile is reduced a second time using microscope optics. This produces the desired pattern of optical traps with a proper beam size at the sample plane.

Experiments demonstrated high-precision generation of various beam profiles that are used to mimic the Laguerre-Gaussian(LG) and Hermite-Gaussian(TEM) beams. Raw measurements of beam profiles at the image feedback arm had a less than 5% RMS error. In addition, we presented dynamic control of the beam profile by rotating and radially transforming the amplitude profile of a LG_{04} mimic beam. In the optical tweezers arm, we demonstrated a cosine-taped ring profile that improved the trap depth compared to a donut (TEM01*) mode that had a shallower trap due to the bandwidth limit of DMD

image projection. This also illustrates that the DMD-based beam shaper is capable of generating any complex optical trap pattern.

Compared to optical traps created by the holographic approach, the DMD-based optical trap has unique advantages with respect to high laser power tolerance, fast operation speed, coherent and incoherent illumination with broadband light sources, and high pattern precision. The major limitation of this approach comes from a comparatively lower energy efficiency and diffraction limited trapping range along the z-axis. In the future, we plan to demonstrate the second-stage image formation of this system and implement it in potential applications of biology, cold atom experiments, and materials science.

7.6 REFERENCES

[1] A. Ashkin, "Acceleration and Trapping of Particles by Radiation Pressure," Phys. Rev. Lett. **24**, 156–159 (1970).

[2] A. Ashkin, J. M. Dziedzic, J. E. Bjorkholm, S. Chu, "Observation of a single-beam gradient force optical trap for dielectric particles," Opt. Lett. **11**, 288–290 (1986).

[3] K. Ladavac, K. Kasza, and D. G. Grier, "Sorting mesoscopic objects with periodic potential landscapes: Optical fractionation," Phys. Rev. E **70**, 010901(2004)

[4] D. R. Albrecht, G. H. Underhill, T. B. Wassermann, R. L. Sah, and S. N. Bhatia, "Probing the role of multicellular organization in three-dimensional microenvironments," Nat. Methods **3**, 369 - 375 (2006).

[5] T. L. Gustavson, A. P. Chikkatur, A. E. Leanhardt, A. Görlitz, S. Gupta, D. E. Pritchard, and W. Ketterle, "Transport of Bose-Einstein Condensates with Optical Tweezers," Phys. Rev. Lett. **88**, 020401 (2001)

[6] D. C. Benito, D. M. Carberry, S. H. Simpson, G. M. Gibson, M. J. Padgett, J. G. Rarity, M. J. Miles and S. Hanna, "Constructing 3D crystal templates for photonic band gap materials using holographic optical tweezers," Opt. Express **16**, 13005 – 13015 (2008).

[7] P. Korda, G. C. Spalding, E. R. Dufresne, and D. G. Grier, "Nanofabrication with holographic optical tweezers," Rev. Sci. Instrum. **73**, 1956 (2002).

[8] C. Liberale, P. Minzioni, F. Bragheri, F. De Angelis, E. Di Fabrizio, And I. Cristiani, "Miniaturized all-fibre probe for three-dimensional optical trappingand manipulation," Nature Photonics, **1** 723-727 (2007).

[9] S. Kawata and T. Sugiura, "Movement of micrometer-sized particles in the evanescent field of a laser beam," Opt. Lett. **17** 772-774 (1992).

[10] M. Righini, G. Volpe, C. Girard, D. Petrov, and R. Quidant, "Surface Plasmon Optical Tweezers: Tunable Optical Manipulation in the Femtonewton Range," Phys. Rev. Lett. **100**, 186804 (2008).

[11] C. H. Sow, A. A. Bettio, Y. Y. G. Lee, F. C. Cheon, C. T. Lim, and F. Watt, "Multiple-spot optical tweezers created with microlens arrays fabricated by proton beam writing," Appl. Phys. B **78**, 705–709 (2004).

[12] Y. Ogura, K. Kagawa, and J. Tanida, "Optical manipulation of microscopic objects by means of vertical-cavity surface-emitting laser array sources," Appl. Opt. **40** 5430-5435 (2001).

[13] R. T. Dame, M. C. Noom, and G. J. L. Wuite, "Bacterial chromatin organization by H-NS protein unravelled using dual DNA manipulation," Nature, **444** 387-390 (2006).

[14] J. E. Curtis, B. A. Koss, D. G. Grier, "Dynamic holographic optical tweezers," Opt. Commun. **207**, 169-175 (2002).

[15] A. Jesacher, C. Maurer, A. Schwaighofer, S. Bernet, and M. Ritsch-Marte, "Full phase and amplitude control of holographic optical tweezers with high efficiency," Opt. Express **16**, 4479-4486 (2008).

[16] L. Paterson, M. P. MacDonald, J. Arlt, W. Sibbett, P. E. Bryant, and K. Dholakia, "Controlled Rotation of Optically Trapped Microscopic Particles," Science **292**, 912-914 (2001).

[17] M. P. MacDonald, L. Paterson, K. Volke-Sepulveda, J. Arlt, W. Sibbett, and K. Dholakia, "Creation and Manipulation of Three-Dimensional Optically Trapped Structures," Science **296** 1101-1103 (2002).

[18] D. Dudley, W. Duncan, J. Slaughter, "Emerging Digital Micromirror Device (DMD) Applications", Proc. SPIE **4985** 14 (2003)

[19] P. Y. Chiou, A. T. Ohta, and M. C. Wu, "Massively parallel manipulation of single cells and microparticles using optical images," Nature, **436**, 370-372 (2005).

[20] J. M. Tam, I. Biran, and D. R. Walt, "Parallel microparticle manipulation using an imaging fiber-bundle-based optical tweezer array and a digital micromirror device," Appl. Phys. Lett. **89**, 194101 (2006).

[21] A. R. Faustov, M. R. Webb, and D. R. Walt, "Note: Toward multiple addressable optical trapping," Rev. Sci. Instrum. **81**, 026109 (2010)

[22] Y. Ren, M. Li, K. Huang, J. Wu, H. Gao, Z. Wang, and Y. Li, "Experimental generation of Laguerre–Gaussian beam using digital micromirror device," Appl. Opt. **49**, 1838 (2010)

[23] A. A. Adeyemi, N. Barakat, and T. E. Darcie, "Applications of digital micro-mirror devices to digital optical microscope dynamic range enhancement," Opt. Express **17**, 1831 (2009).

[24] J. Liang, R. N. Kohn, Jr., M. F. Becker, and D. J. Heinzen, "1.5% root-mean-square flat-intensity laser beam formed using a binary-amplitude spatial light modulator," Appl. Opt. **48**, 1955-1962 (2009).

[25]J. Liang, R. N. Kohn, Jr., M. F. Becker, and D. J. Heinzen, "High-precision laser beam shaping using a binary-amplitude spatial light modulator," Appl. Opt. **49**, 1323-1330 (2010).

[26] V. Ostromoukhov, "A simple and efficient error-diffusion algorithm," Proc. SIGGRAPH 2001, 567-572 (2001).

[27] J. Liang, R. N. Kohn, Jr., M. F. Becker and D. J. Heinzen, "Evaluation of DMD-based high-precision beam shaper using sinusoidal-flattop beam profile generation", Proc. SPIE **8130**, 81300C (2011).

[28] J. Liang, S. Wu, R. N. Kohn, Jr., M. F. Becker and D. J. Heinzen, "Band-limited laser image projection using a DMD-based beam shaper", Proc. SPIE **8254**, 825421 (2012).

[29] C. Alpmann, R. Bowman, M. Woerdemann, M. Padgett, and C. Denz, "Mathieu beams as versatile light moulds for 3D micro particle assemblies," Opt. Express **18**, 26084-26091 (2010)

[30] J. P. Rice, J. E. Neira, M. Kehoe and R. Swanson, "DMD diffraction measurements to support design of projectors for test and evaluation of multispectral and hyperspectral imaging sensors", Proc. SPIE **7210**, 72100D (2009);

[31] R. Beck, J. Parry, R. Carrington, W. MacPherson, et al "Adaptive optics for laser-based manufacturing processes,"

http://www.stfc.ac.uk/resources/pdf/adoppreshand.pdf.

[32] Texas Instrument, "DLP® Discovery™ 4000 Starter Kit Technical Reference Manual," http://focus.ti.com/pdfs/dlpdmd/D4000_TRM%202509931_Preview.pdf.

[33] J. Liang, R. N. Kohn, Jr., M. F. Becker and D. J. Heinzen, "High-precision beam shaper for coherent and incoherent light using a DLP spatial light modulator", Proc. SPIE **7932**, 793208 (2011).

Chapter 8 Conclusion

In this dissertation, we present a beam shaping system based on the digital micromirror device for ultra-cold atom experiments and other potential applications. After evaluation of alternative ways to synthesize a precise beam pattern, an imaging technique that used iterative refinement was selected for development. The precise beam profile generating system started with an error diffusion algorithm that was used to design the first-generation binary DMD pattern based on an accurate measurement of the beam incident on the DMD. Following the DMD, a telescope with a correctly sized pinhole low-pass filtered the flattop beam and scaled it to the desired size. A binary DMD pattern designed by the error diffusion algorithm was then projected to the image plane by a bandwidth-limited 4f telescope that converted the DMD pattern to a grayscale image. A theoretical analysis in the spatial domain revealed that the theoretical limit of image precision for a given system bandwidth was limited by the digitization error. An iterative pattern refinement based on the point spread function (PSF) for the specific system bandwidth was used to seek the lowest possible image error. The blue-noise spectrum of the error diffusion algorithm and the spatial low-pass filtering precisely preserved the target spectrum, which guaranteed high-precision beam shaping performance.

This system was used to produce various beam profiles with different spatial frequency spectra. First, we demonstrated high-precision flattop and other slow-varying intensity beam profiles with 0.20-0.34% RMS error for various coherent and incoherent light sources at different wavelength ranges. This error level is close to the 0.1% RMS error objective, meaning that these beam profiles are suitable for generating the box potential or the homogenous optical lattice for ultracold atoms experiments. The analysis

showed that the overall energy efficiency was mainly determined by diffraction efficiency of the DMD, beam shaping conversion efficiency, and the loss from the device. A LabVIEW automation program was written for fast and automated beam shape control.

Second, the output error level versus system bandwidth for this system was evaluated by using sinusoidal-flattop beam profiles with different spatial periods. Experiments showed that the system performance was close to the theoretical limit with <1% RMS error for normalized system bandwidth $f \leq 1/10.9$; <3% RMS error for $f \leq 1/4.0$. Compared to the error diffusion algorithm, PSF-based iterative pattern refinement provided better image precision for small system bandwidth and similar performance for middle and large bandwidths. Later experiments using a Lena-flattop beam profile demonstrated arbitrary beam profile generation. The quality of output images is subject to the tradeoff between image precision and spatial resolution (or spatial bandwidth). The experiment produced similar RMS errors for different system bandwidths as previous system evaluation. These results indicate that this beam shaping system is capable of generating dynamic optical trap for the ultracold atoms experiment.

This DMD-based beam shaper was implemented for the homogenous optical lattice and dynamic optical trap generation. For homogenous optical lattice generation, the DMD pattern for the flattop beam profile was optimized by the iterative refinement process in the image feedback arm. A two-stage imaging system projected this pattern to the atoms plane and reduced the beam size by 25-50 times. The experiment demonstrated a 1.25% RMS error flattop beam with the diameter of 70.4 μm at the atoms plane. After retro-reflection, the one-dimensional homogeneous optical lattice is formed near the atoms plane. The measurement of the retro-reflected beam profile illustrated good intensity uniformity at the optical lattice. These results indicate that the generated

homogenous 1-D optical lattice is sufficient for use in a quantum emulator using ultracold atoms.

In addition, a dynamic optical trap can be generated by combining this system with a standard inverted microscope. The beam shaping experiment demonstrated various amplitude profiles of Laguerre-Gaussian and Hermite-Gaussian modes (including the donut shape) with approximately 2-4% RMS error. Other experiments verified that this system was capable of generating various desired profiles to optimize the trapping geometry. The DMD-based system has unique advantages of high power tolerance, fast operation speed, coherent and incoherent illumination with broadband wavelengths, and high pattern precision. The major limitation of this approach comes from a relatively low energy efficiency and relatively short trapping range along the longitudinal axis.

In the future, we plan to apply DMD-based beam shaping system to the Bose-Einstein condensate apparatus in the Department of Physics to load ultracold Bosons into the homogenous optical lattice or the box potential to study the phase diagram of the dilute Boson gas and the critical region of the condensate. In addition, we are seeking cooperation for implementing the DMD-based beam shaping system for the potential applications in biology, biomedical engineering, or material science.

Bibliography

[1] J. H. Kelly, L. J. Waxer, V. Bagnoud et al., "OMEGA EP: High-energy petawatt capability for the OMEGA laser facility," Journal De Physique. IV : JP. 133, 75-80.

[2] Sinusoidal MTF Optical Test Chart, Applied Image Inc., http://www.aig-imaging.com/Sinusoidal-MTF-Optical-Test-Chart.html, [Accessed at 2/6/2011].

[3] M. Montes-Usategui, E. Pleguezuelos, J. Andilla, and E. Martín-Badosa, "Fast generation of holographic optical tweezers by random mask encoding of Fourier components," Opt. Express 14, 2101-2107 (2006).

[4] P. F. Van Kessel, L. J. Hornbeck, R. E. Meier, and M. R. Douglass, "A MEMS-based projection display," Proc. IEEE 86, 1687-1704 (1998).

[5] S. Zhang, and P. S. Huang, "High-resolution, real-time three-dimensional shape measurement", Opt. Eng. 45, 123601(2006).

[6] K.B. Davis, M. O. Mewes, M. R. Andrews, N. J. van Druten, D. S. Durfee, D. M. Kurn, and W. Ketterle (1995). "Bose–Einstein condensation in a gas of sodium atoms". Phys.l Rev. Lett. 75 (22)

[7] N. Prokof'ev, O. Ruebenacker, and B. Svistunov, Phys. Rev. A **69**, 053625 (2004).

[8] J. K. Chin, D. E. Miller, Y. Liu, C. Stan, W. Setiawan, C. Sanner, K. Xu, and W. Ketterle, "Evidence for superfluidity of ultracold fermions in an optical lattice,", Nature 443, 961-964 (2006).

[9] W. S. Bakr, J. L. Gillen, A. Peng, S. Fölling, and M. Greiner, "A quantum gas microscope for detecting single atoms in a Hubbard-regime optical lattice", Nature 462, 74-77 (2009).

[10] C. A. Haynam, P. J. Wegner, J. M. Auerbach, M. W. Bowers, S. N. Dixit, G. V. Erbert, G. M. Heestand, M. A. Henesian, M. R. Hermann, K. S. Jancaitis, K. R. Manes, C. D. Marshall, N. C. Mehta, J. Menapace, E. Moses, J. R. Murray, M. C. Nostrand, C. D. Orth, R. Patterson, R. A. Sacks, M. J. Shaw, M. Spaeth, S. B. Sutton, W. H. Williams, C. C. Widmayer, R. K. White, S. T. Yang, and B. M. Van Wonterghem, "National Ignition Facility laser performance status," Appl. Opt. 46, 3276-3303 (2007).

[11] C. Dorrer, S. K.-H. Wei, P. Leung, M. Vargas, K. Wegman, J. Boulé, Z. Zhao, K. L. Marshall, and S. H. Chen, "High-damage-threshold static laser beam shaping using optically patterned liquid-crystal devices," Opt. Lett. 36, 4035-4037 (2011).

[12] C. Dorrer and J. D. Zuegel, "Design and analysis of binary beam shapers using error diffusion," J. Opt. Soc. Am. B 24, 1268–1275 (2007).

[13] D. Zeng, W. P. Latham and A. Kar, "Characteristic analysis of a refractive axicon system for optical trepanning", Opt. Eng. 45, 094302 (Sep 19, 2006).

[14] A. Laskin and V. Laskin, "πShaper – Refractive Beam Shaping Optics for Advanced Laser Technologies" J. Phys.: Conf. Ser. 276 012171 (2011).

[15] J. A. Hoffnagle and C. M. Jefferson, "Design and performance of a refractive optical system that converts a Gaussian to a flattop beam," Appl. Opt. 39, 5488–5499 (2000).

[16] P. J. Smilie and T. J. Suleski, "Variable-diameter refractive beam shaping with freeform optical surfaces," Opt. Lett. 36, 4170-4172 (2011).

[17] J. Menapace, P. Davis, W. Steele, M. R. Hachkowski, A. Nelson, and K. Xin, "MRF applications: on the road to making large-aperture ultraviolet laser resistant continuous phase plates for high-power lasers," Proc. SPIE 6403, 64030N (2006).

[18] C. C. Aleksoff, K. K. Ellis, and B. D. Neagle, "Holographic conversion of a Gaussian-beam to a near-field uniform beam," Opt. Eng. 30, 537–543 (1991).

[19]R. de Saint Denis, N. Passilly, M. Laroche, T. Mohammed-Brahim, and K. Ait-Ameur, “Beam-shaping longitudinal range of a binary diffractive optical element,” Appl. Opt. 45, 8136–8141 (2006).

[20] J. Jia, C. Zhou, X. Sun, and L. Liu, “Superresolution laser beam shaping,” Appl. Opt. 43, 2112–2117 (2004).

[21] T. Ando, Y. Ohtake, N. Matsumoto, T. Inoue, and N. Fukuchi, "Mode purities of Laguerre–Gaussian beams generated via complex-amplitude modulation using phase-only spatial light modulators," Opt. Lett. 34, 34-36 (2009).

[22] V. Bagnoud and J. D. Zuegel, "Independent phase and amplitude control of a laser beam by use of a single-phase-only spatial light modulator," Opt. Lett. 29, 295-297 (2004).

[23] J. S. Liu and M. R. Teghizadeh, “Iterative algorithm for the design of diffractive phase elements for lasr beam shaping”, Opt. Letters 27 (16), 1463-1465 (2002).

[24] H. Ma, Z. Liu, X. Xu, X. Wang, Y. Ma and P. Zhou, “Adaptive generation of a near-diffraction-limited square flattop beam with dual phase only liquid crystal spatial light modulators”, J. Opt. 13 015707 (2011).

[25] A. Kostylev, A. Sobolev, T. Cherezova, and A. Kudryashov, “Genetic algorithm for intracavity laser beam shaping”, Proc. SPIE 5876 587605 (2005).

[26] A. Jesacher, C. Maurer, A. Schwaighofer, S. Bernet, and M. Ritsch-Marte, "Near-perfect hologram reconstruction with a spatial light modulator," Opt. Express 16, 2597-2603 (2008).

[27] M. Pasienski and B. DeMarco, “A high-accuracy algorithm for designing arbitrary holographic atom traps,” Opt. Express 16, 2176–2190 (2008).

[28] H. Zhang, J. Xie, J. Liu, and Y. Wang, "Elimination of a zero-order beam induced by a pixelated spatial light modulator for holographic projection," Applied Optics 48, 5834-5841 (2009).

[29] D. Palima and V. R. Daria, "Holographic projection of arbitrary light patterns with a suppressed zero-order beam," Applied Optics 46, 4197-4201 (2007).

[30] D. W. K. Wong and G. Chen, "Redistribution of the zero order by the use of a phase checkerboard pattern in computer generated holograms," Applied Optics 47, 602-610 (2008).

[31] J. Liang, Z. Cao, and M. F. Becker, "Phase Compression Technique to Suppress the Zero-Order Diffraction from a Pixelated Spatial Light Modulator (SLM)," [Frontiers in Optics, OSA Technical Digest (CD)], Optical Society of America, Washington DC, FThBB6 (2010).

[32] J. Liang, S. Wu, F. K. Fatemi, and M. F. Becker, "Suppression of the Zero-Order Diffracted Beam from a Pixelated Spatial Light Modulator by Phase Compression", submitted to Applied Optics (2012)

[33] "DMD Discovery™ 1100 Controller Board & Starter Kit," http://focus.ti.com/download/dlpdmd/25061976.pdf.

[34] L. J. Hornbeck, "Current Status and Future Applications for DMD™-Based Projection Displays," Proc. 5th Int'l Display Workshops, 1998.

[36] S. Sumriddetchkajorn, "Micromechanics-based digitally controlled tunable optical beam shaper," *Opt. Lett.* 28, 737-739 (2003).

[37] V. Ostromoukhov, "A simple and efficient error-diffusion algorithm," Proc. SIGGRAPH 2001, 567-572 (2001).

[38] K. Knox, "Error image in error diffusion", Proc. SPIE 1657, 268-279 (1992).

[39] M. F. Becker, J. Liang, R. N. Kohn Jr., D. J. and Heinzen, “High-precision laser beam shaping using binary-amplitude DLP spatial light modulators,” Proc. SPIE 7596, 75960A (2010).

[40] J. Liang, R. N. Kohn Jr., M. F. Becker, and D. J. Heinzen, "1.5% root-mean-square flat-intensity laser beam formed using a binary-amplitude spatial light modulator," Appl. Opt. 48, 1955-1962 (2009).

[41] J. Liang, R. N. Kohn Jr., M. F. Becker, and D. J. Heinzen, "High-precision laser beam shaping using a binary-amplitude spatial light modulator," Appl. Opt. 49, 1323-1330 (2010).

[42] J. Liang, R. N. Kohn Jr., M. F. Becker, and D. J. Heinzen, "High-precision beam shaper for coherent and incoherent light using a DLP spatial light modulator", Proc. SPIE 7932, 793208 (2011).

[43] DMD 0.7 XGA 12º DDR DMD Discovery™ Datasheet, http://focus.ti.com/download/dlpdmd/2503686.pdf, access on [1/31/2012]

[44] J. Liang, R. N. Kohn Jr., M. F. Becker, and D. J. Heinzen, "Evaluation of DMD-based high-precision beam shaper using sinusoidal-flattop beam profile generation, " Proc. SPIE 8130, 81300C (2011).

[45] D. Hong, H. Lee, M. Y. Kim, H. Cho, and J. I. Moon, "Sensor fusion of phase measuring profilometry and stereo vision for three-dimensional inspection of electronic components assembled on printed circuit boards," Appl. Opt. 48, 4158-4169 (2009).

[46] M. G. L. Gustafsson, “Nonlinear structured-illumination microscopy: wide-field fluorescence imaging with theoretically unlimited resolution,” Proc. Natl. Acad. Sci. U.S.A. 102, 13081-13086 (2005).

[47] K. Genovese and C. Pappalettere, “Whole 3D shape reconstruction of vascular segments under pressure via fringe projection techniques,” Opt. Laser Eng. 44, 1311-1323 (2006).

[48] J. W. Goodman, “Introduction to Fourier Optics, 3rd ed.”, Roberts & Company Publishers, Chapter 6 (2005).

[49] M. Fujiwara, M. Teshima, J. Kani , H. Suzuki, N. Takachio and K. Iwatsuki, “Optical carrier supply module using flattened optical multicarrier generation based on sinusoidal amplitude and phase hybrid modulation,” J. Lightwave Technol. 21, 2705 - 2714 (2003).

[50] J. Liang, R. N. Kohn, Jr., M. F. Becker, and D. J. Heinzen, “Homogenous 1-D optical lattice generation using a Digital Micromirror Device-based high-precision beam shaper”, J. Micro/Nanolith. MEMS MOEMS 11(2), (2012)

[51] Ophir-Spiricon, LLC, “LBA-FW-SCOR User Manual,” pp. 98 – 99 http://www.ophiropt.com/laser/register_files/lbafwscor.pdf, accessed [2/14/2012].

[52] A. Ashkin, "Acceleration and Trapping of Particles by Radiation Pressure," Phys. Rev. Lett. **24**, 156–159 (1970).

[53] A. Ashkin, J. M. Dziedzic, J. E. Bjorkholm, S. Chu, "Observation of a single-beam gradient force optical trap for dielectric particles," Opt. Lett. **11**, 288–290 (1986).

[54] K. Ladavac, K. Kasza, and D. G. Grier, “Sorting mesoscopic objects with periodic potential landscapes: Optical fractionation,” Phys. Rev. E **70**, 010901(2004)

[55] D. R. Albrecht, G. H. Underhill, T. B. Wassermann, R. L. Sah, and S. N. Bhatia, “Probing the role of multicellular organization in three-dimensional microenvironments,” Nat. Methods **3**, 369 - 375 (2006).

[56] T. L. Gustavson, A. P. Chikkatur, A. E. Leanhardt, A. Görlitz, S. Gupta, D. E. Pritchard, and W. Ketterle, "Transport of Bose-Einstein Condensates with Optical Tweezers," Phys. Rev. Lett. **88**, 020401 (2001)

[57] D. C. Benito, D. M. Carberry, S. H. Simpson, G. M. Gibson, M. J. Padgett, J. G. Rarity, M. J. Miles and S. Hanna, "Constructing 3D crystal templates for photonic band gap materials using holographic optical tweezers," Opt. Express **16**, 13005 – 13015 (2008).

[58] P. Korda, G. C. Spalding, E. R. Dufresne, and D. G. Grier, "Nanofabrication with holographic optical tweezers," Rev. Sci. Instrum. **73**, 1956 (2002).

[59] C. Liberale, P. Minzioni, F. Bragheri, F. De Angelis, E. Di Fabrizio, And I. Cristiani, "Miniaturized all-fibre probe for three-dimensional optical trappingand manipulation," Nature Photonics, **1** 723-727 (2007).

[60] S. Kawata and T. Sugiura, "Movement of micrometer-sized particles in the evanescent field of a laser beam," Opt. Lett. **17** 772-774 (1992).

[61] M. Righini, G. Volpe, C. Girard, D. Petrov, and R. Quidant, "Surface Plasmon Optical Tweezers: Tunable Optical Manipulation in the Femtonewton Range," Phys. Rev. Lett. **100**, 186804 (2008).

[62] C. H. Sow, A. A. Bettio, Y. Y. G. Lee, F. C. Cheon, C. T. Lim, and F. Watt, "Multiple-spot optical tweezers created with microlens arrays fabricated by proton beam writing," Appl. Phys. B **78**, 705–709 (2004).

[63] Y. Ogura, K. Kagawa, and J. Tanida, "Optical manipulation of microscopic objects by means of vertical-cavity surface-emitting laser array sources," Appl. Opt. **40** 5430-5435 (2001).

[64] R. T. Dame, M. C. Noom, and G. J. L. Wuite, "Bacterial chromatin organization by H-NS protein unravelled using dual DNA manipulation," Nature, **444** 387-390 (2006).

[65] J. E. Curtis, B. A. Koss, D. G. Grier, "Dynamic holographic optical tweezers," Opt. Commun. **207**, 169-175 (2002).

[66] A. Jesacher, C. Maurer, A. Schwaighofer, S. Bernet, and M. Ritsch-Marte, "Full phase and amplitude control of holographic optical tweezers with high efficiency," Opt. Express **16**, 4479-4486 (2008).

[67] L. Paterson, M. P. MacDonald, J. Arlt, W. Sibbett, P. E. Bryant, and K. Dholakia, "Controlled Rotation of Optically Trapped Microscopic Particles," Science **292**, 912-914 (2001).

[68] M. P. MacDonald, L. Paterson, K. Volke-Sepulveda, J. Arlt, W. Sibbett, and K. Dholakia, "Creation and Manipulation of Three-Dimensional Optically Trapped Structures," Science **296** 1101-1103 (2002).

[69] D. Dudley, W. Duncan, J. Slaughter, "Emerging Digital Micromirror Device (DMD) Applications", Proc. SPIE **4985** 14 (2003)

[70] P. Y. Chiou, A. T. Ohta, and M. C. Wu, "Massively parallel manipulation of single cells and microparticles using optical images," Nature, **436**, 370-372 (2005).

[71] J. M. Tam, I. Biran, and D. R. Walt, "Parallel microparticle manipulation using an imaging fiber-bundle-based optical tweezer array and a digital micromirror device," Appl. Phys. Lett. **89**, 194101 (2006).

[72] A. R. Faustov, M. R. Webb, and D. R. Walt, "Note: Toward multiple addressable optical trapping," Rev. Sci. Instrum. **81**, 026109 (2010)

[73] Y. Ren, M. Li, K. Huang, J. Wu, H. Gao, Z. Wang, and Y. Li, "Experimental generation of Laguerre–Gaussian beam using digital micromirror device," Appl. Opt. **49**, 1838 (2010)

[74] A. A. Adeyemi, N. Barakat, and T. E. Darcie, “Applications of digital micro-mirror devices to digital optical microscope dynamic range enhancement,” Opt. Express **17**, 1831 (2009).

[75] J. Liang, S. Wu, R. N. Kohn, Jr., M. F. Becker and D. J. Heinzen, "Band-limited laser image projection using a DMD-based beam shaper", Proc. SPIE **8254**, 825421 (2012).

[76] C. Alpmann, R. Bowman, M. Woerdemann, M. Padgett, and C. Denz, "Mathieu beams as versatile light moulds for 3D micro particle assemblies," Opt. Express **18**, 26084-26091 (2010)

[77] J. P. Rice, J. E. Neira, M. Kehoe and R. Swanson, "DMD diffraction measurements to support design of projectors for test and evaluation of multispectral and hyperspectral imaging sensors", Proc. SPIE **7210**, 72100D (2009);

[78] R. Beck, J. Parry, R. Carrington, W. MacPherson, et al “Adaptive optics for laser-based manufacturing processes,”

http://www.stfc.ac.uk/resources/pdf/adoppreshand.pdf.

[79] Texas Instrument, “DLP® Discovery™ 4000 Starter Kit Technical Reference Manual,” http://focus.ti.com/pdfs/dlpdmd/D4000_TRM%202509931_Preview.pdf.

Vita

Jinyang Liang was born in Yueyang, Hunan Province, People's Republic of China on September 16, 1985, the son of Ping Zhou and Jingsha Liang. After completing his work at The First High School of Yueyang in 2003, he entered Beijing Institute of Technology majored in Optoelectronic Engineering the fall of 2003 on a full time basis. In the summer of 2006, he worked as a lab research assistant in Shanghai Institute of Optics and Fine Mechanics, Chinese Academy of Sciences. He graduated with a Bachelor of Engineering Degree in July 2007. In September 2007, he entered the Graduate School of The University of Texas at Austin and received a degree of Master of Science in Engineering under Dr. Michael F. Becker's supervision in 2009. He worked at Digital Light Innovations as an Electrical Engineering student intern since 2011. In the summer of 2010, he participated in Texas 4000 and rode his bike from Austin Texas to Anchorage Alaska to raise money for cancer research.

Permanent Address: Room 4501, Building #14, Longmai Garden
Changping District, Beijing 102211
People's Republic of China

This dissertation is typed by Jinyang Liang.